Particle Methods in Civil Engineering

Treball realitzat per:

Alba Navarro Casanova

Dirigit per:

Antonia Larese

Màster en:

Mètodes Numèrics en Enginyeria

Barcelona, 28 de Setembre 2018

Departament d'Enginyeria Civil I Ambiental, DECA

TREBALL FINAL DE MÀSTER

Particle Methods in Civil Engineering

Author: Alba Navarro Casanova

Internal supervisor: Antonia Larese

Master in Numerical methods

Abstract

This project focuses on particle methods, specifically on the Material Point Method (MPM). MPM is an hybrid mixed Lagrangian-Eulerian method which uses moving Lagrangian material points that store physical properties of a deforming continuum and a fixed Eulerian finite element mesh to solve the equations of motion at each time steps. It has been shown that this method is useful for the simulation of mechanical problems involving large deformations on history-dependent materials.

MPM can be seen as a Lagrangian finite element method with moving integration points (the material points). The main advantages of the Material Point Method, motivates to realize its validation and its application to problems where different materials are in contact and large deformations are involved. Therefore, this thesis focus on the analysis of the MPM methodology, of strengths and weaknesses. To do that, a series of simulations of standardized tests on concrete samples have been carried out. Their experimental behaviour is known and they are easily comparable with the traditional finite elements methods, FEM. Moreover, a preliminary application for the study of the behaviour of the method for the the specific case of the failure of the core of a rockfill dam in extreme conditions.

The study of the method in large deformations regime is done by observing how the push rockfill shoulder and the water affects the dam's core once and it is not protected anymore by the rockfill protection. In this regard, it should be noted that only preliminary analyzes have been carried out so to see the basis of the future research.

Further research is needed to simulate large geotechnical problems such as dam's simulations. For instance, contact algorithm must be implemented to solve stress transmission and friction problems between surfaces when different materials are involved.

Acknowledgment

I would like to thank Antonia Larese, Bodhinanda Chandra and Ilaria Iaconeta for the opportunity to work in a real project applying all the learned concepts during the master. I really appreciate the confidence they put on me since the very beginning and their time and effort dedication.

Finally, I would like to thank to all people that shared their time in one way or other with me; to my family, classmates and all the professors involved in the Numerical Methods Master.

Contents

List of Figures

List of tables

List of Images

1. Introduction and objectives

1.1 Introduction

The needs in the calculation of large structures have been changing. At present, climate change, strong climbs and drops in temperatures, among other extreme conditions, have caused that the efforts acting on these structures have changed, and now they are subject to another conditions and larger forces than the ones contemplated in the past.

Therefore, this need arises to create a method that manages to simulate efforts and behaviours that extreme conditions have on structures. In engineering there exist several problems which involve history-dependent materials, large deformations and complex soil-structure interaction. The numerical simulation of these problems is challenging.

The numerical methods used in continuum mechanics make use of two classical descriptions of motion: the Lagrangian and Eulerian description [17]. In Eulerian methods such as the Finite Differences Methods (FDM), the computational mesh is fixed, and the continuum moves with respect to the grid. Although large deformation problems can be handled with these methods, the Eulerian formulation contains a nonlinear convective term, which makes it hard to deal with history-dependent materials [22]. Traditionally Eulerian methods are used in fluid dynamics.

In Lagrangian methods the mesh follows the material over time, making it easy to follow material free surface or multiple materials [58]. Lagrangian methods are efficient when calculating impact problems because are conceptually simpler, it is easy to impose boundary conditions and track material interfaces (element boundary coincides with material interfaces), and also it is easy to implement history-dependent constitutive models, but still not able to efficiently solve problems where large deformations are considered, because the mesh might get distorted.

The material point method (MPM) tries to combine the advantages of Lagrangian and Eulerian methods. It proved to be successful in simulating problems which involve large deformations and history-dependent materials. MPM uses a fixed background mesh and a set of material points moving through the mesh to model the deforming material. In every time step, the equations of motion are solved numerically on the background mesh to update particle position and properties. The solution is approximated by a linear combination of basis functions. Integrals are approximated using material points as integration points.

The material point method is described as a mesh-based particle method since it uses a background mesh and a set of material points moving through this mesh [1].

One of the earliest mesh-based particle methods is the particle-in-cell (PIC) method developed at Los Alamos National Laboratory by F. H. Harlow for fluid dynamics analyses [28]. In this

method, material points only carry information on mass and position of the continuum not on velocities or stresses. Dissipation of energy is characteristic for this method [10]. A next step was the introduction of the fluid-implicit particle method (FLIP) by Brackbill and Ruppel [10] in 1986. In this method, not only mass and position but also other properties such as momentum and energy are assigned to each particle. It has been shown in [54] that this method conserves kinetic energy if a consistent mass matrix is used.

In 1993, the FLIP method was extended by Sulsky et al. for problems in solid mechanics that involve history-dependent contitutive models [55]. This new method was called the material point method (MPM) by Sulsky and Schreyer [56]. Within MPM, a material is represented by a set of particles where each particle represents a subvolume of the material. Since these material points store physical properties such as stresses and strains, problems involving history-dependent material behavior can easier be simulated. Over the years, the material point method has been used in the simulation of a variety of problems in different fields. For example, it has been used to simulate multiphase flows [58] and the deformation of membranes containing soil [27]. Furthermore, the material point method has been used for snow simulations [53] and to model sea ice dynamics [57].

The objective of this project is to validate the Material Point Method implemented in *Kratos Multiphysics* through various tests carried out. On the other hand, we want to know how the Material Point Method behaves in the fracture of the clay core of a dam in extreme conditions. For this case, only preliminary analyzes have been carried out, the results obtained for now are shown and the future work on the subject is highlighted in order to carry out this type of simulations.

1.2 Objective

The main objective of this work is the validation of the Material Point Method solving for damage problems. For this, several analyses have been carried out using damage models, such as the compression, tensile and shear test in a concrete specimen. An extended comparison with experimental curves with FEM to verify that the method works correctly.

As a future work, since the potential of the MPM relies in the solution of large deformation problems, it is intended to simulate the failure of a rockfill dam under extreme conditions. The model would be a dam in which the core of this has been uncovered and on which the push of the water impacts.

1.3 Thesis outline

The thesis outline is the following: Chapter 1 presents an introduction, some objectives and finally the state of the art.

In the second chapter the mathematical model is described. The governing equations, theories of damage models and the Mohr-Coulomb constitutive law are shown. This chapter also derives the weak form of the problem, its linearization and spatial discretization.

In chapter 3, the subject is introduced, explaining the Material Point Method, the algorithm and the numerical difficulties of this method.

The validation of the method is shown in chapter 4, in which all the tests carried out are exposed and compared and analyzed.

The last chapter is the conclusions that reflect on the work analyzed and the results obtained. Future research lines are also being studied to improve the current method.

2. State of the art

Simulation-based Engineering Science (SBES) is the third pillar of the modern science and engineering [52]. This science has the advantages of low cost, safety, and efficiency in solving various kinds of problems that are presented today.

There are a series of extreme problems that are difficult to solve, such as hypervelocity impact, penetration, blast, crack propagation, and multi-phase (solid–liquid–gas) interactions involving failure evolution, yet effectively discretize localized large deformation, the transition among different types of failure modes and fragmentation remains a very difficult task.

The existing spatial discretization methods can be classified into Lagrangian, Eulerian, and Hybrid ones, depending on the way how deformation and motion are described.

2.1 Lagrangian methods

In these methods the computational grid is embedded and deformed with the material. There is no advection between the grid and material, so no advection term appears in the governing equations, this simplifies the solution process. The mass of each material element keeps constant during the solution process, but due to element deformation the element volume varies.

The main advantages of this methods are:

1) They are conceptually more simple and efficient than Eulerian methods. The conservation equations for mass, momentum, and energy are simple in form (because there is no advection term that describes the mass flow across element boundaries,), and can be efficiently solved.

2) It is easy to impose boundary conditions and to track material interfaces because element boundaries coincide with the material interfaces during the solution process.

3) It is easy to implement history-dependent constitutive models because they track the flow of individual masses.

To obtain a stable solution with an explicit time integration scheme, the time step must be smaller than a critical time step. This critical time step is controlled by the minimum characteristic length of all elements in the grid.

The time step in a Lagrangian calculation could become smaller and smaller, and finally approach zero (because severe element distortion would significantly decrease the characteristic element length), which makes the computation impossible to be completed.

To complete a Lagrangian computation for an extreme loading case, a distorted grid must be remeshed and its result must be interpolated to the remeshed grid.

In 1D and 2D problems the remesh technique has been successfully used, but rezoning a complicated 3D material domain is still a challenging task. For a history-dependent material, the history variables are also required to be interpolated from the old grid to the new grid, which may further cause numerical error in stress calculation.

2.2 Eulerian methods

An Eulerian method is appropriate for problems in which a material domain could become heavily distorted or problems where different materials are mixed.

In these methods, the computational grid is fixed in space and does not move with the material such that the material flows through the grid.

There is no element distortion, but the physical variables, such as mass, momentum, and energy, advect between adjacent elements across their interface.

The volume of each element keeps constant during the simulation, but its density varies due to the advection of mass. These methods are suited for modelling large deformations of materials. Most of computational fluid dynamics codes and early hydrocodes for impact and blast simulation employ these methods.

Eulerian methods only calculate the material quantities advected between elements without explicitly and accurately determining the position of material interface and free surface so that they are quite awkward in following deforming material interfaces and moving boundaries. Significant efforts have been made to develop interface reconstruction methods.

2.3 Hybrid methods

As both Lagrangian and Eulerian methods possess different shortcomings and advantages hybrid methods are the ones which combining both want to take advantage of both methods to better tackle challenging problems. The arbitrary Lagrangian–Eulerian (ALE) [19] method and the particle-in-cell (PIC) method [26, 28] are two representatives.

2.3.1 Arbitrary Eulerian–Lagrangian Method and Its Variations

The ALE method was adopted in the finite element context [6, 31]. The mixed Eulerian-Lagrangian method [21] involves the Eulerian set-up with respect to one dimension and the Lagrangian one to the other dimension which corresponds to the direction of fluid flow.

The code [50] employs an Eulerian mesh for the entire region and Lagrangian meshes for the subregions of fluids with nonstationary boundaries approximated by Lagrangian lines.

These methods can handle a much greater distortion of the material than a Lagrangian method, with a higher resolution than that provided by an Eulerian method, because they offer great flexibility in moving the computational mesh. However, the convective terms still pose some problems and designing an efficient and effective mesh-moving algorithm for complicated 3D problems remains a future task.

2.3.2 Particle-In-Cell Method and Its Variations

In the late 1950's the PIC method was proposed and developed at Los Alamos National Laboratory by Harlow [26, 27, 28]. PIC makes use of both Lagrangian and Eulerian descriptions. The fluid is discretized as a set of Lagrangian particles that carry material position, mass, and species information, but the computational mesh is a uniform Eulerian one.

A computational cycle is divided into two phases:

-The Lagrangian phase: all the variables, including the mesh coordinates and the particle positions, are advanced. This phase updates the quantities by all the processes except for advection.

-The Eulerian (remap or rezone) phase: he mesh is mapped back into its original configuration, leaving the particles at their new locations. This phase moves the particles and accomplishes all of the advective fluxing [30].

As variations of PIC method, some new methods were proposed:

The marker-and-cell (MAC) method was developed by Harlow and Welch [29, 45] to treat incompressible and free surface flows. In this method, particles are used as markers to define the location of the free-surface, and the Poisson equation for the pressure is solved to treat the fluid incompressibility. The MAC method was the first successful technique for simulating incompressible flows [35].

It has to be highlighted that the original version of PIC is not a fully Lagrangian particle method because only the material position, mass, and species information is carried by the particles, while the remaining quantities are still stored in the computational grid. This transfer of information between the particles and the background grid produces a significant numerical diffusion.

To reduce the numerical diffusion are two strategies: a second-order accuracy advection scheme [49] and fully Lagrangian particle method. A fully lagrangian particle method was developed by Brackbill, called FLuid-Implicit-Particle (FLIP) method [9, 10], in which each particle carries all of the properties of the fluid, including momentum and energy. The FLIP method preserves the

ability of the original PIC to resolve contact discontinuities, but eliminates this major source of numerical diffusion.

2.3.3 Material Point Method

In 1990, Zhen Chen and Buck Schreyer wanted to improve the computational fidelity and efficiency of the finite element method (FEM), due to its limitation in the required use of a pin-hole in the mesh design. In a seminar Deborah Sulsky presented the advances of the PIC method, based on her collaborative research on computational fluid dynamics with the scientists at *Los Alamos National Laboratory*. Since the particle motion in fluid is similar to the penetrator's motion in solid from the viewpoint of hard–soft body interaction. This aspect opened a new direction of research and started an interdisciplinary discussion.

In collaboration with Sandia National Laboratories, the team started to combine computational fluid dynamics with computational solid dynamics to develop a continuum-based particle method with its first journal paper published in 1994 [55], which was later named as the Material Point Method (MPM). Over the last two decades, many research teams in the world have further developed the MPM and combined the MPM with other numerical methods for multiphase, multiphysics, and multiscale simulations to advance SBES.

2.4 Meshfree Methods and many prominent features of the MPM.

In addition to the evolution of the MPM, different types of meshfree and particle methods for improved spatial discretization in different problems have also been proposed and developed in the SBES community.

Since all these meshfree and particle methods do not use a rigid mesh connectivity compared with the conventional mesh-based methods such as the FEM, they have been applied to many problems of current interests (e.g. impact/contact, localization, crack propagation, penetration, perforation, fragmentation, ...)

But many of the meshfree methods have a higher computational costs, and the accuracy of some meshfree methods is still dependent on the node regularities.

One of the earliest meshfree Lagrange particle methods is the Smoothed particle hydrodynamics (SPH). The SPH was first proposed by Lucy [14] and Gingold and Monaghan [32] in 1977 to solve astrophysical problems in the 3D open space, and has been extensively studied and extended to solid and fluid dynamics problems with large deformations.

Both the SPH and its improved versions have been successfully applied to the hypervelocity impact simulations. This method become some of the most popular meshfree methods in this

area. But it has a negative point, and it is that it is limited in simulating multiphase interactions involving failure evolution.

The SPH basic formulation and features were compared with the ones of MPM through a comparative study [12], thhis comparative study showed that the MPM possesses many prominent features:

→ The formulation of the MPM is simple and similar to the traditional FEM.
→ The time consuming neighbor searching, which is compulsory in most meshfree methods, is not required in the MPM.
→ The MPM shape functions exactly satisfy the constant and linear consistency.
→ The MPM avoids tensile instability that is annoying in the SPH.
→ The boundary conditions can be applied in the MPM as easily as in the FEM, and the contact algorithm can be efficiently implemented whose cost is linear in the number of material points involved. Because the same regular computational grid can be used in all time steps, the time step keeps constant in the MPM simulations. Numerical studies have showed that the computational efficiency and stability of the three-dimensional MPM code are much higher than those of SPH.

2.5 Recent studies on the subject.

The material point method is described as a mesh-based particle method since it uses a background mesh and a set of material points moving through this mesh.

One of the earliest mesh-based particle methods is the particle-in-cell (PIC) method developed at Los Alamos National Laboratory by F. H. Harlow for fluid dynamics analyses. In this method, material points only carry information on mass and position of the continuum not on velocities or stresses. Dissipation of energy is characteristic for this method. A next step was the introduction of the fluid-implicit particle method (FLIP) by Brackbill and Ruppel in 1986. In this method, not only mass and position but also other properties such as momentum and energy are assigned to each particle. It has been shown that this method conserves kinetic energy if a consistent mass matrix is used.

In 1993, the FLIP method was extended by Sulsky for problems in solid mechanics that involve history-dependent constitutive models. This new method was called the material point method (MPM) by Sulsky and Schreyer. Within MPM, a material is represented by a set of particles where each particle represents a subvolume of the material. Since these material points store physical properties such as stresses and strains, problems involving history-dependent material behaviour can easier be simulated.

In 2000 a model for granular materials was presented by S.G. Bardenhagen, J.U. Brackbill and D.Sulsky [4]. This model describes both the internal deformation of each granule and the interactions between grains. It is based on the FLIP-material point and particle-in-cell method (PIC) and solves continuum constitutive models for each grain. Interactions between grains are calculated with a contact algorithm that forbids interpenetration, but allows separation and

sliding and rolling with friction. The goal of this method was not only to allow each grain to deform according to continuum constitutive models, but also to describe the interactions between grains, including separation, sliding, and rolling. It was used an Eulerian grain-level continuum model. Finite difference approximations to the continuum equations were solved on an Eulerian mesh. Material interfaces were resolved by Interface tracking. In the development was considered that friction between grains is 0. The contact mixture theory was ensuresing the proper traction boundary conditions along the boundary. Therefore, it was argued that precise modelling of particle deformation was not necessary to obtain a good approximation of the mechanical behavior.

In 2001 was developed an improved contact algorithm for the MPM and the application to stress propagation in granular material [5]. There, a new approach to contact was implemented using the MPM for solid mechanics. Bardenhagen, Brackbill and Sulsky described two improvements to the algorithm: include the normal traction in the contact logic to more appropriately determine the free separation criterion, and provide a numerical stability by scaling the contact impulse when the information of the computational grid is suspicious. This new approach takes advantage of MPM which tracks Lagrangian particle motion through an Eulerian grid. An essential modification to the physics of the algorithm is described, as well as a modification for numerical stability.

Lagrangian bodies are discretized into material points, which carry all information required to specify the current state and advance the solution. This information includes constitutive parameters (such as moduli and internal variables), stress, strain, velocity and temperature. The governing equations are solved on the grid, providing a computational saving and as well as regular, structured grid on which to apply solution techniques. Quantities are interpolated between the mesh and the material points such the total mass and momentum are conserved. Conservation of mass is satisfied implicitly in MPM. Material points are assigned fixed masses during the initial discretization. Conservation of momentum is solved on the grid and changes are interpolated to material points such that the change in momentum is the same on the grid and on the material points. Contact is modeled on the computational grid. With this analysis was shown that MPM provides a convenient framework for the implementation of contact between deformable bodies. The contact calculations were computationally efficient, performed on the computational grid body by body, without requiring a search to identify neighbors.

A potential numerical difficulty associated with unfortunate registration of particle information on the computational grid had been eliminated by scaling which retains both the efficient properties of the algorithm, and conservation of momentum during contact. As future work they consider focusing on obtaining better measurements of the parameters, comparing simulation to experiment quantitatively, and simulating more complex assemblages.

A little later, in 2002 Zhen Chen presented "An evaluation of the material point method" [13] , in which he made a detailed discussion on the treatments of boundary conditions and shock wave problems. Performed a direct inspection of the two-dimensional MPM code. A one-dimensional MPM code was programmed to solve one-dimensional wave and impact problems, with linear elasticity and elastoplasticity models. The advantages and disadvantages of MPM

were investigated compared to mesh-free methods. In addition, future research directions were discussed to better simulate complex physical problems such as impact / contact, location, crack propagation and interactions between different material phases, among others.

Z. Chen concludes that the key difference among different spatial discretization methods is how the gradient and divergence terms are calculated, meshless methods do not use a rigid mesh connectivity as compared with the FEM, FDM and BEM, the interpolation in the moving domain of influence is the common feature of the meshless methods.

Although a background mesh is used to calculate the gradient and divergence terms, the MPM is still based on the interpolation in the moving domain of influence, namely, the spatial discretization is continuously adjusted as a body deforms. Thus, the MPM can be considered as one of the meshless methods, understanding meshless in the sense that a rigid mesh connectivity is not used in spatial discretization. In comparison with the other meshless methods, the MPM appears to be less complex with a cost factor of at most twice that associated with the use of corresponding finite elements. Due to the mapping from material points to cell nodes and the mapping from cell nodes to material points involved in each time step, the MPM can simulate localized large deformations without mesh tangling. The use of the same set of continuous shape functions in both mappings results in a natural no-slip contact/impact scheme so that no inter-penetration would occur.

In 2003 J.A. Nairn describe a CRAMP algorithm which extends MPM to naturally handle explicit cracks [48]. Conventional MPM enforces velocity and displacement continuity through its background grid. This approach is incompatible with cracks which are displacement and velocity discontinuities. By allowing multiple velocity fields at special nodes near cracks, the new method (CRAMP) can model cracks. When the fracture code is written efficiently, especially the new line crossing section, the code achieves crack calculations with very letter extra cost in calculation time.

It is shown that CRAMP gets the correct MPM solutions and comparisons to both FEA and experiments show that it gets good results for crack problems. The method to detect crack contact is robust for internal cracks but may need some adjustment for problems involving edge cracks. The important problem that remains is the calculation of crack tip or fracture parameters followed by prediction of crack propagation. This problem will be the subject of future work and also an extension to 3D.

In 2003 was developed and implemented an implicit integration strategy for use with the material point method (MPM) [24]. An incremental-iterative solution strategy was developed around Newton's method to solve the equations of motion with Newmark integration to update the kinematic variables.

The implicit MPM solutions were compared directly with those obtained using an explicit MPM code and implicit finite element (FE) code. The accuracy of the implicit solution was superior to the explicit MPM when compared to validated FE solutions, and by definition the implicit time integration is unconditionally stable. Similarities between the assembly of the implicit MPM

equations and those of the FE method were identified and should allow further algorithmic improvement. The implicit FEM will likely continue to be faster even after optimization as the IMPM (and EMPM) requires several additional interpolation steps between the particles and the computational grid that are not necessary with implicit FEM.

In 2004 . Z. Wiezckowski developed an analysis of the material point method in large strain engineering problems [62]. The method was enriched by adding the more accurate procedure evaluating the volume change of the analysed body which was making some problems, e.g. silo filling, possible to solve.

Some problems like granular flow around a silo insert and the problem of self-contact of granular material could be solved in relatively easy way by the use of the material point method in contrast to the standard finite element method. The material point method looked very promising as a tool of analysis of other large strain problems like motion of avalanches and simulation of earth-moving processes. However, the method was time consuming and Z. Wiezckowski belived that the use of parallel computation technique could reduce the time consumption of the method.

In 2006 it has been realized an analisis of the discrete and continuum modelling of silo discharge [15]. The Discrete Element Method (DEM) is used for discrete modelling and the Material-Point Method (MPM) for continuum modelling. Standard finite element methods have difficulty in modelling the complete discharge process unless remeshing is employed. It was shown with some experiments that the use of meshless methods was overcoming this problem. DEM and MPM simulations were performed and the results of flow patterns and flow rates compared to experiments. It was concluded that both DEM and MPM can successfully model the total discharge process in terms of flow patterns and flow rates. A time study shown that if a relatively small number of particles were used in a DEM model, the computing times were comparable to that of MPM.

More later, in 2013 Zhen Chen studied the Combination of the MPM with Other Methods for Multi-physics and/or Multi-scale Simulation. He thought that the MPM could be combined with other numerical methods for multi-physics and multi-scale simulations in different cases with the least computational costs.

MD simulations were performed to predict coupled rate and size effects at nanoscale, which provide the useful information for formulating an effective multi-scale equation of state.

A multi-scale simulation procedure was developed, via hierarchical approach from MD to CD/rDPD and concurrent one between CD/rDPD and MPM, for modeling and simulating energetic composite responses, in combination with in-lab experiments.

In 2013, in the 18th Conference for Soil Mechanics and Geotechnical Engineering (Paris) was presented the Material Point Method as a promising computational tool in Geotechnics [2]. The dynamic formulation of the MPM was exposed and the capability of the method was demonstrated to analyze in a unified mathematical framework the static-dynamic transition of a slope failure.

In 2015 Ming Gong developed his doctoral thesis on Improving the MPM [23]. The attention of his work was focused on the convergence properties of MPM in terms of order of accuracy and stability. In his thesis was shown numerically that MPM was losing convergence and was suffering cell crossing errors for large deformation problems. Two remedies were proposed: the generalized interpolation material point method (GIMP) and the convected particle domain interpolation method (CPDI). Both GIMP and CPDI try to improve MPM by altering the geometry of the evolved material-point domain. Such changes lead to improvement of the quadrature part of the MPM algorithm. In this sense there is shown a different approach to improving MPM by combining ideas from meshfree particle methods and finite element methods. Such an approach provides a general framework for improving MPM.

One year later, R. Tielen presented a thesis of a high order material point method [60]. In MPM, the integrals resulting from the variational formulation used to solve the background grid are numerically approximated by using the material points as integration points. When the material points become unevenly distributed inside the mesh, some errors were generated because the quality of the numerical quadrature rule is not accurate enough. In this thesis was shown a way to improve the quality of this numerical quadrature rule when this situation occurs. In MPM is a common practice to adopt piecewise linear basis functions to approximate the solution of the variational form. A problem arises from the discontinuity of the gradients of these basis functions at element boundaries. Such grid crossing errors significantly affect the quality of the numerical solution and may lead to a lack of spatial convergence. As a remedy to these problems in this thesis was presented a version of the MPM making use of quadratic B-spline basis functions is presented. The C^0-continuity of their gradients eliminates grid crossing errors. This in turn results in lower computational effort. To improve spatial convergence, the use of a consistent mass matrix instead of a lumped one commonly used with the MPM is suggested to project velocities from material points to the grid more accurately.

Also in 2016, J. Tao, Y. Zheng, Z. Chen and H. Zhang investigated a generalized interpolation material point method for coupled thermo-mechanical processes, GIMP [59]. This method born for simulating coupled thermo-mechanical processes is developed based on the weak formulations of both conservation of momentum and conservation of energy. To imrpove the accuracy of GIMP was proposed a multi-grid approach in dealing with the Dirichlet boundary conditions in thermal analyses. It was shown that the proposed procedure might provide a robust spatial-discretization tool for multi-physics simulations.

In 2016 was presented a comparison of a displacement-based and a stabilized mixed formulation within the framework of the Material Point Method [47]. A standard Galerkin displacement-based formulation was compared with a stabilized mixed formulation, where displacement and mean stress were considered as primary variables, within the framework of an implicit Material Point Method (MPM). Many works in the previous literature had demonstrated that, under the assumption of elastic and plastic near incompressibility or incompressibility, a displacement-based formulation was not able to evaluate in the correct way the deviatoric strain field, producing the volumetric locking of the solid under analysis and leading to non-physical results of the displacement and stress fields. In the study, a

stabilized mixed formulation for solid mechanics problem was implemented in a MPM code and validated throughout classical solid and soil mechanics benchmark examples. It was demonstrated that the mixed formulation was able to evaluate more accurate results not only under near incompressible, but also under compressible conditions.

On January of 2017. Y. G. Motlagh and W. M. Coombs propose an Implicit high order MPM [37]. As we have said before despite the MPM being promoted for its ability to solve large deformation problems the method suffers from instabilities when material points cross between elements. These instabilities are due to the lack of smoothness of the grid basis functions used for mapping information between the material points and the background grid. In this paper as R. Tielen, they performed a novel high-order MPM in order to eliminate the cell-crossing instability and improve the accuracy of the MPM method.

In 2017, S. Kularathna and K. Soga developed a projection method in material point method for modelling incompressible materials [8]. They presented an implicit MPM formulation based on Chorin's projection method for solving incompressible material problems. And they shown the capability of the implicit MPM formulation to solve fully incompressible material problems. Specially, the implicit formulation allows a large time step compared to the significantly small time step in explicit MPM formulation at near incompressible conditions.

Also in 2017, Y. Bing, M. Cortis, T. Charlton, W. Coombs and C. Augarde investigated a boundary representation and boundary condition imposition in the material point method [36]. In their study a B-spline based boundary approximation method is discussed. A local cubic interpolation technique is employed for boundary representation. Tractions are applied through direct integration over the B-spline boundary and displacements are prescribed via a B-spline based implicit boundary method.

Later in the same year, E. G. Kakouris, S. P. Triantafyllou present a phase-field material point method for brittle fracture [14]. The material point method for the analysis of deformable bodies is revisited and originally upgraded to simulate crack propagation in brittle media. In this setting, phase-field modelling is introduced to resolve the crack path geometry. Following a particle in cell approach, the coupled continuum/phase-field governing equations are defined at a set of material points and interpolated at the nodal points of an Eulerian, ie, non-evolving, mesh. The accuracy of the simulated crack path is thus decoupled from the quality of the underlying finite element mesh and relieved from corresponding mesh-distortion errors. A staggered incremental procedure is implemented for the solution of the discrete coupled governing equations of the phase-field brittle fracture problem. The proposed method is verified through a series of benchmark tests while comparisons are made between the proposed scheme, the corresponding finite element implementation, and experimental results.

Also Z. P. Chen, X. Zhang, X. M. Qiu and Y. Liu developed a frictional contact algorithm for implicit material point method [32]. The explicit material point method (MPM) works successfully in modeling high frequency problems, but it is very computationally expensive in simulating low frequency with small time steps or quasi-static problems.

Thus, they have developed an implicit MPM for modeling low frequency problems. Recently, a few attempts were undertaken to investigate the contact problems using the implicit MPM but the accuracy was dissatisfactory.

An augmented Lagrange formulation for the frictional inequality constraints is introduced. A discretization of the Lagrange multiplier field based on the background grid is proposed to establish the implicit MPM framework with the contact algorithm. To reduce the complexity of the solution, the Uzawa algorithm is employed to decouple the unknown variables and the Lagrange multipliers. Finally, the resulting sequent nonlinear equations are solved by the Newton method, in which the tangential matrix is assembled explicitly. By using the compressed sparse row (CSR) technique, the total storage of the matrix can be greatly reduced. Numerical studies show that the computational efficiency and accuracy of the implicit MPM with the proposed contact algorithm are much higher than the explicit MPM.

In 2017, CIMNE compared the material point method and the galerkin meshfree method for the simulation of cohesive-frictional materials [33]. The simulation of large deformation problems, involving complex history-dependent constitutive laws, is of paramount importance in several engineering fields.

In the study a Material Point Method (MPM) and a Galerkin Meshfree Method (GMM) were presnetd and verified against classical benchmarks in solid mechanics.

The aim was to demonstrate the good behavior of the methods in the simulation of cohesive-frictional materials, both in static and dynamic regimes and in problems dealing with large deformations. The techniques proposed in this work were based on implicit approaches, which can also be easily adapted to the simulation of static cases.

The two methods were presented so as to highlight the similarities to rather than the differences from "standard" Updated Lagrangian (UL) approaches commonly employed by the Finite Elements (FE) community.

Although both methods were able to give a good prediction, it was observed that, under very large deformation of the medium, GMM lacks robustness due to its meshfree nature, which makes the definition of the meshless shape functions more difficult and expensive than in MPM. On the other hand, the mesh-based MPM was demonstrated to be more robust and reliable for extremely large deformation cases.

The objective in CIMNE is to get an implicit code because although they are more complicated, more expensive, they are more accurate, and stability does not depend on the wave propagation speed in the media. An implicit MPM can solve from static and quasi static to dynamic and gravity driven problems. This is more robust and more "FEM like".

The objective is to develop a numerical tool in the continuum mechanics framework for the simulation of granular flows at the macroscale focusing on dry granular material in static and flowing regime. This tool has to be able to handle large deformation and displacement and to handle history dependent material, With good conservation properties, parallelizable and modular (multiphase, multimaterial…)

Last year I. Iaconeta, A. Larese, R. Rossi and E. Oñate developed an implicit material point method applied to granular flows [34]. The main objective of this work was the development of a variational implicit Material Point Method (MPM), implemented in the open source Kratos Multiphysics framework. The ability of the MPM technique to solve large displacement and large

deformation problems is widely recognised and its use ranges over many problems in industrial and civil engineering.

In the current work the continuum based implicit MPM is applied to engineering applications, where granular material flow is involved.

For the resolution of the length and time scale of these particular problems, both continuum and discrete models are typically used. Even if discrete techniques predict more feasible results, nowadays, their use is limited to the investigation of element tests of particles, or to the simulation of reduced systems, not allowing to make important decisions in the analysis and design of granular processes.

During this study, some advantages of MPM over discrete methods were tested, such as, the ability to simulate granular flow at the large scale with acceptable computational cost and the capability to get information of stress and strain state in a more straightforward way.

This year a soil-structure interaction simulation of landslides impacting a structure using an implicit material point method is presented by B. Chandra, A. Larese, I. Iaconeta, R. Rossi and R. Wüchner [12]. A soil-structure interaction simulation based on the implicit material point method (MPM) has been implemented within the Kratos Multiphysics framework for the objective of predicting structural deformation and, furthermore, structural failure caused by environmental flow problems such as landslides. In the current study, the soil is modeled using a non-associated Mohr-Coulomb-based elastoplastic law, while the structure is modeled as elastic and Neo-Hookean hyperelastic materials.

In the numerical tests conducted, the equivalent stress and displacement measured on both rigid and flexible structures show a good qualitative agreement. In the future works, a more adequate consideration of the soil and structural model will be investigated before conducting a real-scale landslide simulation.

3. Methodology

In this chapter a short overview of continuum mechanics theory is provided as required in this thesis. For a detailed treatment, the reader is referred to [15]. At the beginning a description of the Eulerian and Lagrangian frame of reference used to describe the motion of a continuum is presented. After that, several definitions and the governing equations are introduced.

3.1 Lagrangian vs. Eulerian

As it is said in the introduction different frames of reference can be adopted to observe the motion of a continuum. In the Eulerian frame of reference, a control volume is considered with a fixed position in time. Material is able to move in and out of the control volume. Conservation equations for mass and momentum in describe the inflow and outflow of both mass and momentum into and out of the control volume which must be equal to the change of mass and momentum inside the control volume.

In the Lagrangian frame of reference, a control volume is followed as it moves with time. The control volume always contains the same set of material and can deform in time. Conservation equations for mass and momentum are derived by using the fact that both mass and momentum of this control volume remain constant.

The two frames of reference are illustrated in Figure 1. Note that in the Eulerian frame of reference, material can move in and out of the control volume. Therefore the 'walls' of the control volume are permeable. In a Lagrangian frame of reference, this is not the case. If the control volumes are assumed to be infinitely small, this leads to conservation equations in differential form. In this thesis the Lagrangian frame of reference is considered.
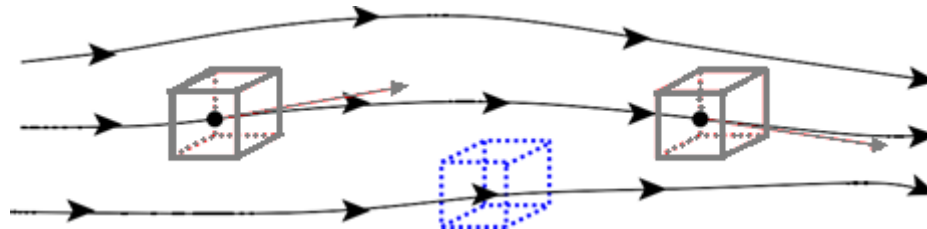

Figure 1: The Lagrangian (grey) and Eulerian (blue) approach illustrated [59].

3.2 Motion and Kinematics

Consider the deformation of a continuum with initial domain Ω_0 at time $t = 0$ s. The configuration Ω_t represents the state of the continuum after deformation at time t and will be referred to as

the current configuration. The movement of a material point at initial position **X** ∈ Ω₀ to the position **x** ∈ Ωₜ can be written as:

$$x = x(X, t) \tag{1}$$

Figure2 illustrates the initial and deformed configuration of a continuum for the 2D case. The function **x(X**, t) has a unique inverse denoted by **X(x**, t) which gives the initial position of a point situated at position **x** at time t. The displacement **u(X**, t) at time t of a point intially located at position **X** is then defined by:

$$u(X, t) = x(X, t) - X(x, t) \tag{2}$$

Velocities and accelerations can be obtained from displacements by taking the total derivative with respect to t :

$$v(X, t) = \frac{du}{dt}(X, t) \tag{3}$$

$$a(X, t) = \frac{dv}{dt}(X, t) \tag{4}$$

In the Eulerian description, the material derivative of a quantity *F(x, t)* can be obtained by using the chain rule :

$$\frac{DF(x, t)}{Dt} = \frac{\partial F(x, t)}{\partial t} + \frac{\partial F(x, t)}{\partial x} \cdot \frac{\partial x(X, t)}{\partial t} = \frac{\partial F(x, t)}{\partial t} + v \cdot \nabla F(x, t)$$

The first term on the right-hand side of equation is the **local derivative** or **Eulerian derivative**, which yields the local rate of change of the quantity occurring at position **x**. The second term of the right-hand side is the **convective derivative** that expresses the rate of change of the quantity contributed by the particle motion due to the nonuniformity of the quantity in space. The material derivative establishes a link between the Eulerian description and Lagrangian one of continuum deformation.

By following the motion of material points, the Lagrangian description can readily track material interfaces and implement history-dependent material models so that it is commonly used in solid mechanics.
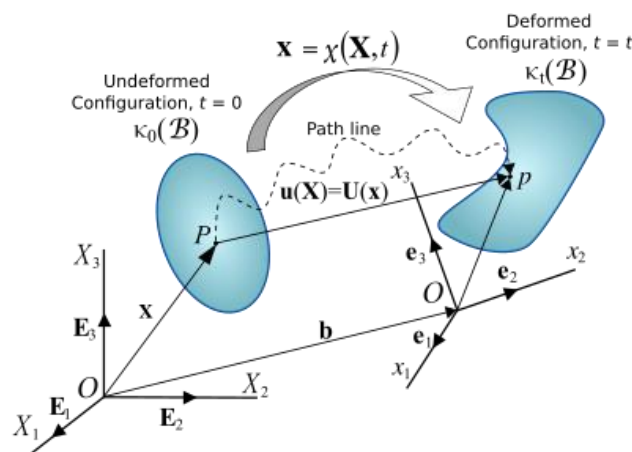
The strain tensor $\boldsymbol{\varepsilon}$ in incremental form is defined in the following way:

$$\frac{\partial \boldsymbol{\varepsilon}_{(i,j)}}{\partial t} = \frac{1}{2}\left(\frac{\partial \mathbf{v}_i}{\partial \mathbf{x}_j} + \frac{\partial \mathbf{v}_j}{\partial \mathbf{x}_i}\right) \tag{6}$$

where $i, j \in \{1,2,3\}$. It defines strain increments with respect to the undeformed state.

3.3 Governing Equations

Consider the body $\mathcal{B}$, which occupies a region Ω of the three-dimensional Euclidean space $\mathcal{E}$ with a regular boundary $\partial\Omega$ in its reference configuration. The deformation of this body, $\mathcal{B}$ is described by a one-to-one mapping:

$$\varphi: \Omega \rightarrow \mathcal{E} \tag{7}$$

which maps each point $\boldsymbol{p}$ of the body B into a spatial point **x**:

$$x = \varphi(\boldsymbol{p}) \tag{8}$$

This equation represents the location of $\boldsymbol{p}$ in the deformed configuration of the body, $\mathcal{B}$. The region of $\mathcal{E}$ occupied by $\mathcal{B}$ in its deformed configuration is denoted as $\varphi(\Omega)$.

This problem is governed by mass and linear momentum balance equations, shown below:

$$\frac{D\rho}{Dt} + \rho\nabla \cdot v = 0 \quad in \quad \varphi(\Omega) \tag{9a}$$

$$\rho a - \nabla \cdot \sigma = \rho b \quad in \quad \varphi(\Omega) \tag{9b}$$

where ρ is the mass density, a is the acceleration, v is the velocity, σ is the symmetric Cauchy stress tensor and b is the body force.

By definition, acceleration and velocity are the material derivatives of the velocity, v, and the displacement, u, respectively. If it is the case of a compressible material, the conservation of mass is fulfilled by:

$$\rho = \frac{\rho_0}{\det(\boldsymbol{F})} \tag{10}$$

Where ρ_0 is the density in the undeformed configuration and $\det(\boldsymbol{F})$ is the determinant of the total deformation gradient $\boldsymbol{F} = dx/d\mathrm{X}$ with x and X representing respectively the current and initial position.

The previous equation (10) holds at any point and at the sampling points where the equation is written, e.g., the material points. As thermal effects are not considered in this work the energy balance is considered fulfilled.

The balance equations are solved numerically in a three-dimensional region $\Omega \subseteq \mathrm{R}^3$, in the time range t $\in$ [0, T], given the following boundary conditions on the Dirichlet $(\varphi(\partial\Omega_D))$ and Neumann boundaries $(\varphi(\partial\Omega_N))$, respectively:

$$u = \bar{u} \quad on \quad \varphi(\partial\Omega_D) \tag{11a}$$

$$\sigma \cdot n = \bar{t} \quad on \quad \varphi(\partial\Omega_N) \tag{11b}$$

where n is the unit outward normal.

In spite of everything is needed a constitutive equation for evaluate the stress-strain relation and to fully define the boundary value problem.

The stress tensor, σ takes the following form in 3D:

$$\sigma = \begin{bmatrix} \sigma_{(1,1)} & \sigma_{(1,2)} & \sigma_{(1,3)} \\ \sigma_{(2,1)} & \sigma_{(2,2)} & \sigma_{(2,3)} \\ \sigma_{(3,1)} & \sigma_{(3,2)} & \sigma_{(3,3)} \end{bmatrix}$$

The nine components of the stress tensor define the stresses acting on a single point completely. Figure 3 denotes the different components of the stress tensor.

3.4 Constitutive relation

3.4.1 Damage Models: The classical uniaxial damage theory

Within the classical approach a very simple measure of the damage amplitude in a given plane is obtained by measuring the area of the intersection of all defects with that plane. For example, based on Figure 3, it   is readily observed that the effective area of the sample subjected to uniaxial tension is S – SD. SD represents the defects trace in the considered plane. The following positive scalar ω is then commonly considered as a damage

$$\omega = \frac{S_D}{S} \tag{12}$$

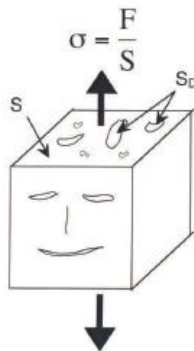variable in the above 1D experiment:

<div align="center">**Figure 3: Cross section of damage material [39].**</div>

For the undamaged material, SD = 0 and then ω = 0. The damage being related to the growth of defects, ω may grow from 0 to a critical value often taken in literature equal to 1 which corresponds to an entirely damaged material (effective area S – SD reduced to 0). Instead of the standard uniaxial stress $\sigma = \frac{F}{S}$, it is convenient to introduce for the damaged material the effective stress:

$$\tilde{\sigma} = \frac{F}{S - S_D} = \frac{F}{S(1 - \frac{S_D}{S})} = \frac{\sigma}{1 - \omega} \tag{13}$$

in which use has been made of (12). Associated to a strain equivalence principle, the 1D effective stress $\tilde{\sigma}$ is related to the elastic strain of the material by the uniaxial Hooke's law :

$$\tilde{\sigma} = E\varepsilon \tag{14}$$

where E is the elastic modulus of the undamaged material. It follows that the constitutive law for the standard stress σ takes the form:

$$\sigma = (1 - \omega)E\varepsilon \tag{15}$$

For the uniaxial model formulation, equation (15) must be completed by the damage evolution law which can be considered in the form of a dependence between the damage variable ω and the applied load:

$$\omega = g(\varepsilon) \tag{16}$$

A priori, the function g can be identified from uniaxial tension test. It must be noted that the relation between ω and ε is valid only in the monotonous loading regime. In an unloading and reloading phase, the damage variable kept its maximum value reached before. A classical way to describe in a unified manner these different loading regimes consists in introducing a variable κ which characterizes the maximum level of strain reached in the material before the current time t : κ(t) = max ε(τ) for τ ≤ t. The damage evolution relation (16) can then be recast in the form:

$$\omega = g(\kappa) \tag{17}$$

which remains valid for any kind of loading regime. The complete elastic response of the damaged material is schematized in Figure 4. Instead of considering the function g, it is usual to introduce a limit state function:

$$f(\varepsilon, \kappa) = \varepsilon - \kappa \tag{18}$$

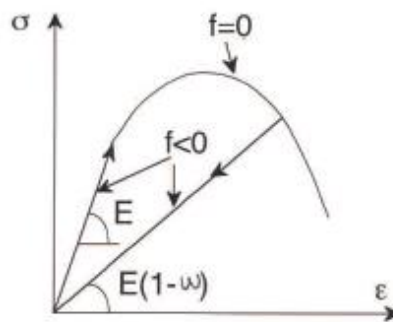Figure 4: Elastic response of a damage material during loading-unloading [39].

Equation (18) is completed by the classical Kuhn-Tucker condition:

$$f \leq 0; \ \dot{\kappa} \geq 0; \ \dot{\kappa}f = 0 \tag{19}$$

The condition f ≤ 0 indicates that ε can never be greater than κ, while the second condition means that κ cannot decrease. Besides, the second condition implies that κ can increase only if

the current value of the strain is equal to κ. In summary, the basic elements of the above uniaxial damage theory are as follows:

-the stress-strain law: $\sigma = E_s \varepsilon = (1 - \omega)E\varepsilon$; this relation appears as a classical Hooke's law with a secant modulus $E_s = (1 - \omega)E$ associated to the damaged material. A simple determination of the damage variable is then: $D = 1 - \frac{E_s}{E}$. It requires however a careful and accurate measure the elastic strain, a damage evolution law which can be put in the form $\omega = g(\kappa)$ or a limit state function f; a first approach can consist to choose $f(\varepsilon, \kappa) = \varepsilon - \kappa$.

3.4.2 Damage models

3.4.2.1 A simple isotropic damage theory

A straightforward 3D extension of the previous uniaxial theory is given by J. Lemaitre [38] 3D elastic damage model. In this model, based on the various concepts presented in section 3.4.1 , it is postulated that the stiffness D of the damaged material reads:

$$\mathbb{D} = (1 - \omega)\mathbb{D}_0 \tag{20}$$

in which D_0 denotes the elastic stiffness of the undamaged material and ω is defined by (1). It is readily seen that the generalization of the uniaxial stress-strain constitutive law (15) takes the form:

$$\underline{\underline{\sigma}} == (1 - \omega)\mathbb{D}_0 : \underline{\underline{\varepsilon}} \tag{21}$$

and the corresponding effective stress tensor $\tilde{\sigma}$ is given by

$$\underline{\underline{\sigma}} == (1 - \omega)\overline{\underline{\underline{\sigma}}} \tag{22}$$

In the present three-dimensional formulation of the isotropic damage model, only the Young modulus is affected, the Poisson ratio remains constant during the damage process. This is clearly a shortcoming of this simple model and will be corrected in section 3.

Let us come now to the 3D loading function f and to the damage evolution. F defines in the 3D strain space the domain of elasticity whose boundary corresponds to the strain states at which the damage will evolve. An immediate generalization of (18) reads:

$$f\left(\underline{\underline{\varepsilon}}, \kappa\right) = \varepsilon_{eq}\left(\underline{\underline{\varepsilon}}\right) - \kappa \tag{23}$$

in which the equivalent strain ε_{eq} is a norm of ε that needs to be chosen. A first simple choice for this can be:

$$\varepsilon_{eq} = \sqrt{\underline{\underline{\varepsilon}} : \underline{\underline{\varepsilon}}} \tag{24}$$

Another choice can be the elastic energy (function of the strain): $\varepsilon_{eq} = \sqrt{\underline{\underline{\varepsilon}} : \mathbb{D}_0 : \underline{\underline{\varepsilon}}}$

3.4.3.2 An isotropic damage modelling of concrete materials

The two norms of ε introduced before for the definitions of ε_{eq} leads to a symmetric elastic domain in tension and compression. However, several materials (rocks, concrete, ceramics) often show a dissymetric damage surface, the yield value in compression being several times the value in tension. To overcome these limitations, [44] introduced two damage parameters, ω_t associated to a tension mechanism and ω_c devoted to the damage under compression. These two parameters, ω_t and ω_c, are evaluated from two evolution functions, g_t and g_c, which are assumed to depend both on a unique definition of the equivalent strain :

3.4.3.3 Background

The influence of microcracking due to external loads is introduced via a single scalar damage variable d ranging from 0 for the undamaged material to 1 for completely damaged material. The stress-strain relation reads:

$$\varepsilon_{ij} = \frac{1 + \mathcal{V}_0}{E_0(1 - d)}\sigma_{ij} - \frac{\mathcal{V}_0}{E_0(1 - d)}\left[\sigma_{kk}\delta_{ij}\right] \tag{25}$$

E0 and v0 are the Young's modulus and the Poisson's ratio of the undamaged material; ε_{ij} and σ_{ij} are the strain and stress components, and δ_{ij} is the Kronecker symbol. The elastic (i.e., free) energy per unit mass of material is

$$\rho\psi = \frac{1}{2}(1 - d)\varepsilon_{ij}C_{ijkl}^0\varepsilon_{kl} \tag{26}$$

where C_{ijkl}^0 is the stiffness of the undamaged material. This energy is assumed to be the state potential. The damage energy release rate is

$$Y = -\rho\frac{\partial\psi}{\partial d} = \frac{1}{2}\varepsilon_{ij}C_{ijkl}^0\varepsilon_{kl} \tag{27}$$

with the rate of dissipated energy:

$$\dot{\boldsymbol{\phi}} = -\frac{\partial\rho\psi}{\partial d}\dot{\boldsymbol{d}} \tag{28}$$

Since the dissipation of energy ought to be positive or zero, the damage rate is constrained to the same inequality because the damage energy release rate is always positive.

3.4.3.4 Evolution of damage

The evolution of damage is based on the amount of extension that the material is experiencing during the mechanical loading. An equivalent strain is defined as

$$\tilde{\varepsilon} = \sqrt{\sum_{i=1}^{3}(\langle\varepsilon_i\rangle_+)^2} \tag{29}$$

where $\langle.\rangle_+$ is the Macauley bracket and ε_i are the principal strains. The loading function of damage is

$$f(\tilde{\varepsilon}, \kappa) = \tilde{\varepsilon} - \kappa \tag{30}$$

where κ is the threshold of damage growth. Initially, its value is κ_0, which can be related to the peak stress f_t of the material in uniaxial tension:

$$\kappa_0 = \frac{f_t}{E_0} \tag{31}$$

In the course of loading k assumes the maximum value of the equivalent strain ever reached during the loading history.

If $f(\tilde{\varepsilon}, \kappa) = 0$ and $\dot{f}(\tilde{\varepsilon}, \kappa) = 0,$ $then$

$$\begin{bmatrix} d = h(\kappa) \\ \\ \kappa = \tilde{\varepsilon} \end{bmatrix} with\ \dot{d} \geq 0, else \begin{bmatrix} \dot{d} = 0 \\ \\ \dot{\kappa} = 0 \end{bmatrix} \tag{32}$$

The function $h(\kappa)$ is detailed as follows: in order to capture the differences of mechanical responses of the material in tension and in compression, the damage variable is split into two parts:

$$d = \alpha_t d_t + \alpha_c d_c \tag{33}$$

where d_t and d_c are the damage variables in tension and compression, respectively. They are combined with the weighting coefficients α_t and α_c, defined as functions of the principal values of the strains ε_{ij}^t and ε_{ij}^c due to positive and negative stresses:

$$\varepsilon_{ij}^t = (1-d)C_{ijkl}^{-1}\sigma_{kl}^t, \qquad \varepsilon_{ij}^c = (1-d)C_{ijkl}^{-1}\sigma_{kl}^c \tag{34}$$

$$\alpha_t = \sum_{I=1}^{3}\left(\frac{\langle \varepsilon_i^t \rangle \langle \varepsilon_i \rangle}{\tilde{\varepsilon}^2}\right)^{\beta}, \quad \alpha_c = \sum_{I=1}^{3}\left(\frac{\langle \varepsilon_i^c \rangle \langle \varepsilon_i \rangle}{\tilde{\varepsilon}^2}\right)^{\beta} \tag{35}$$

Note that in these expressions, strains labeled with a single indicia are principal strains. In uniaxial tension α_t=1 and $\alpha_c = 0$. In uniaxial compression α_c=1 and $\alpha_t = 0$. Hence, d_t and d_c can be obtained separately from uniaxial tests.

3.4.4 Mohr Coulomb material model

If the shear stress at a point on any plane within a soil becomes equal to the shear strength, failure will occur at that point. The shear strength τ_f was expressed by Coulomb as a linear function with cohesion c, angle of shearing φ and normal stress at failure σ_f. As shear stresses in

a soil body can be resisted only by the skeleton of solid particles, this expression should be defined in terms of effective stresses as

$$\tau_f = c' + \sigma_f' \tan \phi' \tag{36}$$

Equation (36) reveals that failure will occur at any point in the soil where a critical combination of shear stress and effective normal stress develops. It is important for the interpretation of shear strength parameters to know that shear resistance is developed by inter-particle forces. If the normal effective stress is zero, then the shearing resistance is zero and the effective cohesion would be zero as well. These parameters are merely constants defining a linear relationship between shear strength and effective normal stress (Craig, 2004) [16].

It is possible to represent states of stress in two dimensions as a plot of shear stress τ against the effective normal stress σ'. A stress state can be defined either in a Mohr circle by the major principal stress σ_1' and the minor principal stress σ_3', or by a point with coordinates τ and σ'. In 2D space, the failure envelope symbolizes the straight or slightly curved line touching the Mohr circle or stress points as shown in Figure 5. A stress point or a Mohr circle part that lies above the envelope cannot exist. At stress ranges within the yield locus, the soil material is elastic in its behaviour.

As a critical combination of shear stress and effective normal stress develops, the stress point will coincide with the failure envelope and a perfectly plastic material behaviour is assumed, with continuous shearing at constant stress. Once a perfectly plastic state has been reached, the material can never return to a fully elastic behaviour without any irrecoverable deformations.

The Mohr-Coulomb failure criterion can be expressed as

$$\sigma_1' = \sigma_3' \tan^2\left(45 + \frac{\phi'}{2}\right) + 2c' \tan\left(45 + \frac{\phi'}{2}\right) \tag{37}$$

and determines what critical combination of effective principal stresses that give rise to a failure condition, Craig (2004) [16].
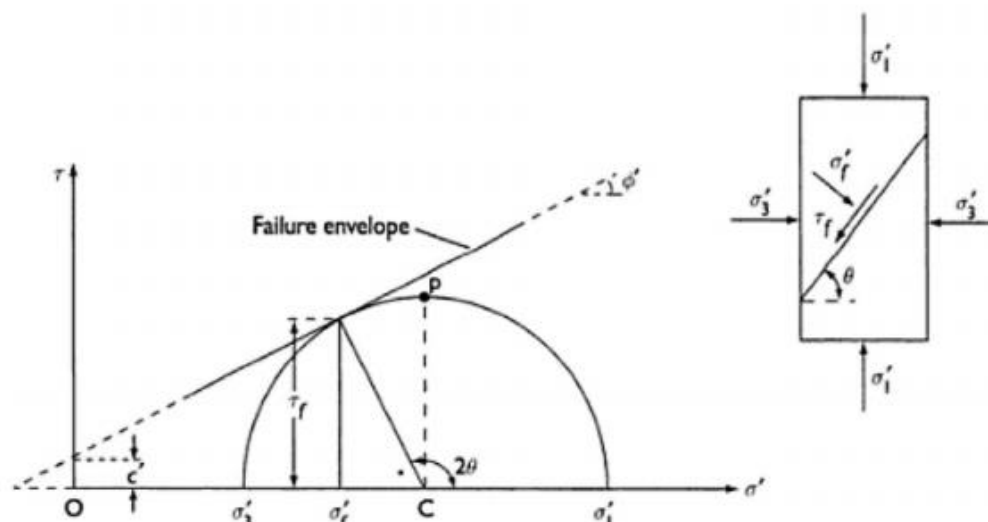

Figure 5: Mohr-Coulomb failure criterion and envelope [16].

3.5 Weak form of the problem

In Section 3.3, has been defined the strong form of the problem. In this part, is going to be derived the weak form. If the formulation explained in [65] is followed, it is obtained a displacement-based finite element procedure.

Let the displacement space $\mathcal{V} \in [\mathbf{H}^1 (B)]^d$ be the space of vector functions whose components and their first derivatives are square-integrable; the integral form of the problem is:

$$\int_{\varphi(\Omega)} (\nabla \cdot \sigma) \cdot w \, dv + \int_{\varphi(\Omega)} \rho(\boldsymbol{b} - \boldsymbol{a}) \cdot w \, dv - \int_{\varphi(\partial\Omega_N)} (\sigma \cdot n - \mathcal{F}) \cdot w \, da = 0, \qquad (38)$$

$$\forall w \in \mathcal{V}$$

where w is an arbitrary test function, such $w = \{w \in \mathcal{V} | \, w = 0 \, on \, \varphi(\partial\Omega_D)\}, dv$ is the differential volume and da the differential boundary surface. By integrating by parts, considering the symmetry of the stress tensor and applying the divergence theorem, the following expression is obtained:

$$\int_{\varphi(\Omega)} \sigma : (\nabla^S w) dv - \int_{\varphi(\Omega)} \rho(b - a) \cdot w \, dv - \int_{\varphi(\partial\Omega_N)} \bar{t} \cdot w \, da = 0 \qquad (39)$$

Assuming the stress tensor is a function of the current strain only:

$$\sigma = \sigma(\epsilon) \qquad (40)$$

the problem is reduced to find a kinematically-admissible field $\boldsymbol{u}$ that satisfies:

$$G(\boldsymbol{u}, w) = 0 \quad \forall w \in \boldsymbol{\mathcal{V}} \qquad (41)$$

where G is the virtual work functional defined as:

$$G(u, w) = \int_{\varphi(\Omega)} \sigma : (\nabla^S w) dv - \int_{\varphi(\Omega)} \rho(b - a) \cdot w \, dv - \int_{\varphi(\partial\Omega_N)} \mathcal{F} \cdot w \, da \qquad (42)$$

3.5.1 Linearization of the Spatial Weak Formulation

In this work, we attempt to solve the general Boundary Value Problems (BVP), characterized by both geometrical and material non-linearity. When a non-linear BVP is considered, the discretisation of the weak form results in a system of non-linear equations; for the solution of such a system, a linearization is, therefore, needed. The most used and known technique is Newton–Raphson's iterative procedure, which makes use of directional derivatives to linearize the non-linear equations.

The virtual work functional of Equation (42) is linearized with respect to the unknown **u**, using an arbitrary argument u^*, which is chosen to be the last known equilibrium configuration.

The linearized problem is to find δu such that:

$$L(\delta u, w) \cong G(u^*, w) + DG(u^*, w)[\delta u] = 0 \qquad \forall w \in \mathcal{V} \tag{43}$$

where L is the linearized virtual work function and:

$$DG(u^*, w)[\delta u] = \frac{d}{d\gamma}\bigg|_{\gamma=0} G(u^* + \delta u, w) \tag{44}$$

is the directional derivative of G at u^* in the direction of $d\boldsymbol{u}$, given by:

$$DG(u^*, w)[\delta u] = \frac{d}{d\gamma}\bigg|_{\gamma=0} \int_{\varphi(\Omega)} [\sigma(\epsilon(\gamma)) : (\nabla^S w) - \rho(b-a) \cdot w]dv$$

$$- \frac{d}{d\gamma}\bigg|_{\gamma=0} \int_{\varphi(\Omega_N)} \mathcal{F} \cdot w \, da \qquad (45)$$

Under the assumption of conservative external loads, only the terms related to the internal and inertial forces are dependent on the deformation. Using the following definitions:

$$\epsilon(\gamma) = \nabla^S(u^* + \gamma\delta u) = \epsilon^* + \gamma\nabla^S(\delta u) \tag{46}$$

Where $\epsilon^* = \nabla^S(u^*)$ is the strain field at u^* and $u(\gamma) = u^* + \gamma\delta u$, the directional derivative DG $(u^*, w)[\delta u]$ reduces to:

$$DG(u^*, w)[\delta u]$$

$$= \frac{d}{d\gamma}\bigg|_{\gamma=0} \int_{\varphi(\Omega)} [\sigma(\epsilon(\gamma)) : (\nabla^S w) - \rho a(u(\gamma)) \cdot w]dv = DG^{static}(u^*, w)[\delta u]$$

$$+ DG^{dynamic}(u^*, w)[\delta u] \tag{47}$$

which can be split into a static and dynamic contribution.

Under the assumption of finite strains and adopting an updated Lagrangian kinematic framework, the expression of the directional derivative (Equation (47)) should be derived in spatial form.

A common way to do that consists of linearizing the material weak form and in doing a push-forward operation to recover the spatial form [65]. Therefore, the linearization of the weak form derived with respect to the initial configuration reads:

$$DG(u^*, w)[\delta u] = \int_{\Omega} \nabla_X \delta u S \cdot \nabla_X w \, dV + \int_{\Omega} [(F^T \nabla_x^S w F) : \mathbb{C}(F^T \nabla_x^S \delta u F)]dV$$

$$+ \int_{\Omega} \rho_0 \frac{da}{du}$$

$$\cdot w[\delta u]dV \tag{48}$$

Where ∇_X and ∇_x are the material and spatial gradient operator, respectively, S is the second Piola-Kirchhoff stress tensor, $\mathbb{C}$ is the fourth order incremental constitutive tensor and dV is the differential volume element in the undeformed configuration. The linearization of the weak form

with respect to the current configuration can be derived by pushing forward the linearization of Equation (48). The first term can be directly written in terms of the Kirchhoff $\tau = FSF^T$ as:

$$\nabla_X \delta u S \cdot \nabla_X w = \nabla_X \delta u F^{-1} \tau F^{-1} \cdot \nabla_X w \tag{49}$$

And using this standard identity $\nabla_X a = \nabla_X a F^{-1}$, Equation (17) can be written as

$$\nabla_X \delta u S \cdot \nabla_X w = \nabla_x \delta u \tau \cdot \nabla_x w \tag{50}$$

The second integral of Equation (47) can be re-written as:

$$\int_\Omega \nabla_x^S w : \mathbb{C}[\nabla_x^S \delta u] \, dV \tag{51}$$

adopting the transformation of the fourth order incremental constitutive tensor C in Voigt notation [65]:

$$\hat{\mathbb{C}}_{iklm} = F_{iA} F_{IC} F_{mD} F_{kB} \mathbb{C}_{ABCD} \tag{52}$$

where lowercase indexes refer to the incremental constitutive tensor relative to the Kirchhoff stress, while uppercase indexes to the incremental constitutive tensor relative to the second Piola–Kirchhoff stress.

With these transformations, the linearization of the static contribution at the current configuration is:

$$DG^{static}(u^*, w)[\delta u] = \int_\Omega \nabla_x \delta u \tau \cdot \nabla_x w + \nabla_x^S w : \hat{\mathbb{C}}[\nabla_x^S \delta u] dV \tag{53}$$

Considering the definition of the determinant of the deformation gradient:

$$\det(F) = J = \frac{dv}{dV} \tag{54}$$

the following relations hold

$$\sigma = \frac{1}{J} \tau \tag{55}$$

$$\bar{\mathbb{C}} = \frac{1}{J} \hat{\mathbb{C}} \tag{56}$$

where $\boldsymbol{\sigma}$ and $\boldsymbol{\tau}$ are the Cauchy and Kirchhoff stress tensor, respectively, and $\bar{\mathbb{C}}$ is the incremental constitutive tensor relative to the Cauchy stress. Equation (48) can now be re-written in the current configuration as:

$$DG(u^*, w)[\delta u] = \int_{\varphi(\Omega)} \left(\nabla_x \delta u \sigma \cdot \nabla_x w + \nabla_x^S w : \bar{\mathbb{C}}[\nabla_x^S \delta u] + \rho \frac{da}{du} \cdot w[\delta u] \right) dv \tag{57}$$

Equation (57) represents the linearization of the spatial weak formulation, also known as the updated Lagrangian formulation, since the deformation state u^* is continuously updated during the non-linear incremental solution procedure, e.g., Newton–Raphson's method.

3.5.2 Spatial Discretisation

For the sake of clarity, hereinafter, the p subscript is used to refer to variables attributed to the material points, while the I subscript is used to refer to variables attributed to the computational nodes.

Let us assume discretizing the continuum body B by a set of n_p material points and assigning a finite volume of the body Ω_p to each of those material points. Thus, the geometrical representation (B_h) of B reads:

$$\mathcal{B} \approx \mathcal{B}_h = \bigcup_{p=1}^{n_p} \Omega_p \tag{58}$$

and the integrals of the weak form can be written as:

$$\int_{\mathcal{B}} (\dots)dV \approx \int_{\mathcal{B}^h} (\dots)dV = \bigcup_{p=1}^{n_p} \int_{\Omega_p} (\dots)d\Omega_p \tag{59}$$

Let $\mathcal{V}_h$ be a finite element space to approximate $\mathcal{V}$. The problem is now finding $u_h \in \mathcal{V}_h$ such that:

$$DG(u_h^*, w_h)[\delta u_h] = -G(u_h^*, w_h), \quad \forall w_h \in \mathcal{V}_h \tag{60}$$

Or using Equation (57):

$$\int_{\varphi(\Omega)} \left\{ \nabla_x \delta u_h \sigma \cdot \nabla_x w_h + \nabla^S w_h : \bar{\bar{\mathbb{c}}}[\nabla^S \delta u_h] + \rho \frac{da_h}{du_h} \cdot w_h[\delta u_h] \right\} dv$$

$$= -\left(\int_{\varphi(\Omega)} \sigma : (\nabla^S w_h)dv \right.$$

$$\left. - \int_{\varphi(\Omega)} \rho(b - a_h) \cdot w_h dv - \int_{\varphi(\partial\Omega_N)} \mathcal{F} \cdot w_h da \right) \tag{61}$$

The detailed procedure to obtain the linearization of Equation (60) can be found in [65]. The final discretized form can be written as:

$$\bigcup_{P=1}^{n_p} \sum_{I=1}^{n} \sum_{K=1}^{n} w_1^T \left((\nabla_x N_I)^T \sigma (\nabla_x N_K) I + B_I^T D B_K + \frac{N_I \rho N_K}{\beta \Delta t^2} I \right) V_p \delta u_K$$

$$= -\bigcup_{P=1}^{n_p} \sum_{I=1}^{n} w_1^T \left(B_I \sigma - \rho b N_I + \sum_{K=1}^{n} N_I \rho N_K a_K \right) V_p$$

$$- \bigcup_{l=1}^{n_t} \sum_{l=1}^{n_m} w_I^T N_I \mathcal{F} A_l \tag{62}$$

where I and K are the indexes of the finite element's nodes, $\nabla_x N_I$ is the spatial gradient of the shape function evaluated at node I, $\mathbf{D}$ is the matrix form of the incremental constitutive tensor $\overline{\overline{\mathbb{c}}}$, V_p is the volume relative to a single material point, A_l is the surface and $\boldsymbol{B}_I$ is the deformation matrix relative to node I, expressed here for a 2D problem as:

$$B_I = \begin{bmatrix} \dfrac{\partial N_I}{\partial x} & 0 \\ 0 & \dfrac{\partial N_I}{\partial y} \\ \dfrac{\partial N_I}{\partial y} & \dfrac{\partial N_I}{\partial x} \end{bmatrix} \tag{63}$$

The left-hand side of Equation (61) is given by three addends multiplied by the increment of the unknowns. The first one is commonly known as the geometric stiffness matrix:

$$K_{IK}^{geo} = (\nabla_x N_I)^T \sigma (\nabla_x N_K) I V_P \tag{64}$$

While the second term is known as the material stiffness matrix:

$$K_{IK}^{mat} = B_I^T D B_K V_p \tag{65}$$

And their sum represents the static contribution to the tangent stiffness matrix:

$$K_{IK}^{static} = K_{IK}^{geo} + K_{IK}^{mat} \tag{66}$$

The dynamic component is given by

$$K_{IK}^{dynamic} = \frac{N_I \rho N_K}{\beta \Delta t^2} I V_p \tag{67}$$

and its definition depends on the adopted time scheme as explained in Section 3.6.
Finally, the tangent stiffness matrix is given by:

$$K_{IK}^{tan} = K_{IK}^{static} + K_{IK}^{dynamic} \tag{68}$$

And represents the submatrix relative to one node of the discretisation with dimension $[n_{dof} \times n_{dof}]$, where n_{dof} is the number of degrees of freedom of a single node. The matrix can be considered as the Jacobian matrix of the right-hand side of Equation (61), i.e., the residual $\mathbf{R_I}$. Equation (61) can be rewritten in compact form as:

$$K_{IK}^{tan} \delta u_K = -\mathbf{R_I} \tag{69}$$

3.6 Material Point Method formulation

The material point method is introduced in this section as a numerical method to solve problems involving large deformations. MPM is a particle method that was proposed for the first time by Harlow [28] in order to solve fluid flow problems under a large deformation regime and originally known by the name of the Particle-In-Cell (PIC) method.

Some time later, Sulsky and coworkers presented its extension to solid mechanics problems [55, 58] As previously commented, most MPM codes use explicit time schemes, which are generally better when simulating fast transient problems or impacts at high velocities.

In cases where the driving force is gravity or when the rate of deformation is small, the best choice is the use of an implicit time scheme because the stability of the method does not depend on the wave propagation speed within the media, which provides the typical time step limitation for explicit approaches [61]. We use an implicit MPM. In the development of this work, the displacement-based formulation and the time scheme integration of the MPM algorithm are equal (equivalent) to those proposed by [23].
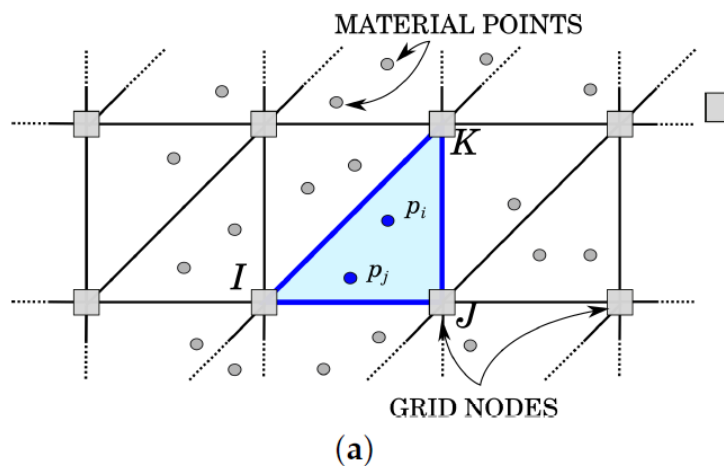
Figure 3: Shape functions calculation in MPM. The shape functions on the material point pi are evaluated using the FE shape function of the element I-J-K [33].

In general the MPM algorithm is structured in three different phases [58], that are graphically represented in Figure 4:

(a) The first phase is the **Initialization phase** (Figure 4a): At the beginning of the time step, the connectivity is defined for each material points, and the initial conditions on the FE grid nodes are created by means of a projection of material points' information obtained at the previous time step t_n;

(b) The second phase is the **UL-FEM calculation phase** (Figure 4b): The local matrix, represented by the left-hand-side (lhs) of Equation (61), and the local vector, constituted by the right-hand-side (rhs) of Equation (61), are evaluated in the current configuration according to the formulation presented in the previous section. The global left-hand-side matrix (LHS) and the global right-hand-side vector (RHS) are obtained by assembling the local contributions of each material point, and finally, the system is iteratively solved. During the iterative procedure, the nodes are allowed to move, according to the nodal solution, and the material points do not change their local position within the geometrical element until the solution has reached convergence;

(c) And the third phase is the **Convective phase** (Figure 4c): During the third and last phase, the nodal information at time t_{n+1} is interpolated back to the material points. The position of the material points is updated and, in order to prevent mesh distortion, the undeformed FE grid is recovered.

MPM and the finite element method have many features and characteristics in common [48]. Actually, Phase b correspond with the calculation step of a standard non-linear FE code, while Phases a and c define the MPM features.

During Phase a, at the beginning of each time step (t_n), the degrees of freedom and the variables on the nodes of the fixed mesh are defined gathering the information from the material points (Figure 4a).
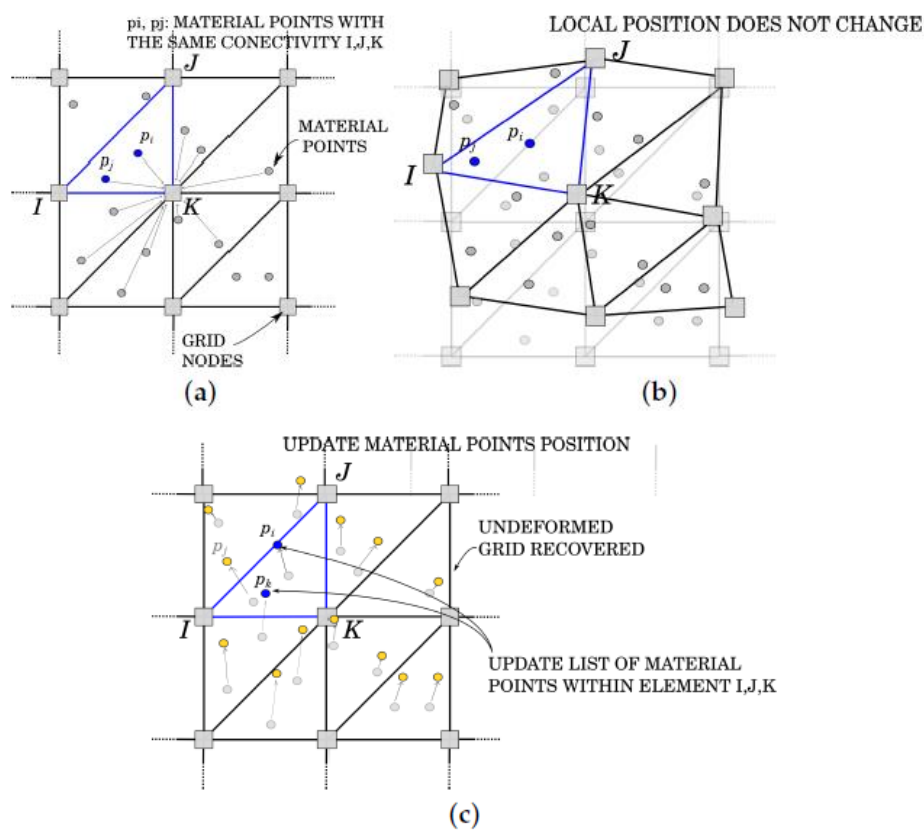
Figure 4: MPM phases (a) Initialization phase; (b) Updated Lagrangian FEM phase; (c) Convective phase [33].

The boundary conditions can be applied in the MPM as easily as in the FEM. In MPM boundary conditions (e.g. prescribed displacement) are imposed to the background grid, whereas the external force and initial velocity are applied on the particles. For example, in a 3D problem, essential boundary conditions can be applied on the six faces of the 3D background grid (e.g. displacement=0 at the bottom), but the forces and velocities must be applied on the material particles.

The momentum q_p and inertia f_p on the material points, which are defined as functions of mass m_p, velocity v_p and acceleration a_p:

$$q_p^n = v_p^n m_p \tag{70}$$
$$f_p^n = a_p^n m_p \tag{71}$$

are projected on the background grid by evaluating in a first step the global values of nodal mass m_I momentum q_I and inertia q_I as described in MPM algorithm.

Once m_I, q_I and f_I are obtained, it is possible to compute the values of nodal velocity and nodal acceleration of the previous time step as:

$$\widetilde{v_I^n} = \frac{q_I^n}{m_I} \tag{72}$$

$$\widetilde{a_I^n} = \frac{f_I^n}{m_I} \tag{73}$$

It is worth mentioning that the initial nodal conditions are evaluated at each time step using material point information in order to have initial values even on grid elements empty at the previous time step ($t_{n-1} - t_n$).

Both Lagrangian techniques presented in this paper make use of a predictor/corrector procedure, based on the Newmark integration scheme.
In MPM, the prediction of the nodal displacement, velocity and acceleration reads:

$$^{it+1}\Delta u_I^{n+1} = 0.0 \tag{74}$$

$$^{it+1}v_I^{n+1} = \frac{\lambda}{\zeta \Delta t}\left[\;^{it+1}\Delta u_I^{n+1}\right] - \left(\frac{\lambda}{\zeta} - 1\right)\widetilde{v_I^n} - \frac{\Delta t}{2}\left(\frac{\lambda}{\zeta} - 2\right)\widetilde{a_I^n} \tag{75}$$

$$^{it+1}a_I^{n+1} = \frac{1}{\zeta \Delta t^2}\left[\;^{it+1}\Delta u_I^{n+1}\right] - \frac{1}{\zeta \Delta t}\widetilde{v_I^n} - \left(\frac{1}{2\zeta} - 1\right)\widetilde{a_I^n} \tag{76}$$

where the upper-left side index it indicates the iteration counter, while the upper-right index n the time step. *l* and *z* are Newmark's coefficients equal to 0.5 and 0.25, respectively.

Once the nodal velocity and acceleration are predicted (Equations (73)–(75)), the system of linearized governing equations is formulated, according to Section 3.5, and the local matrix $\boldsymbol{K}^{tan}$ and the residual $\boldsymbol{R_I}$ are evaluated and assembled according to Equations (61) and (68), respectively (Phase b, Figure 4b).

The solution in terms of increment of nodal displacement is found iteratively solving the residual-based system of Equation (68). Once the solution $^{it+1}\delta u_I^{n+1}$ is obtained, a correction of the nodal increment of displacement is performed:

$$^{it+1}\Delta u_I^{n+1} = \;^{it}\Delta u_I^{n+1} + \;^{it+1}\delta u_I^{n+1} \tag{77}$$

Velocity and acceleration are corrected according to Equations (74) and (75), respectively.

This procedure has to be repeated until convergence is reached.

Unlike an FEM code, the nodal information is available only during the calculation of a time step: at the beginning of each time step, a reset of all the nodal information is performed, and the accumulated displacement information is deleted. The computational mesh is allowed to deform only during the iterative procedure of a time step, avoiding the typical element tangling of a standard FEM. When convergence is achieved, the position of the nodes is restored to the original one (Phase c, Figure 4c). Before restoring the undeformed configuration of the FE grid, the solution in terms of nodal displacement, velocity and acceleration is interpolated on the material points, as:

$$\Delta u_p^{n+1} = \sum_{n=1}^{n_n} N_I(\xi_p, \eta_p)\, \Delta u_I^{n+1} \tag{78}$$

$$a_p^{n+1} = \sum_{n=1}^{n_n} N_I(\xi_p, \eta_p)\, a_I^{n+1} \tag{79}$$

$$v_p^{n+1} = v_I^n + \frac{1}{2}\Delta t\left(a_p^n + a_p^{n+1}\right) \tag{80}$$

where n_n is the total number of nodes per geometrical element, (ξ_p, η_p) are the local coordinates of material point p and $N_I(\xi_p, \eta_p)$ is the shape function evaluated at the position of the material point p, relative to node I.

Finally, the current position of the material points is updated as:

$$x_p^{n+1} = x_p^n + \Delta u_p^{n+1} \tag{81}$$

MPM algorithm is presented in detail in the section MPM algorithm.

3.5.1 MPM algorithm
(we will use $(\bullet)^n = (\bullet)(t_n)$)

Material DATA: $E, \mathcal{V}, \rho$

Initial data on material points: $m_p, \mathbf{x}_p^n, \Delta t, \mathbf{u}_p^n, \mathbf{v}_p^n, \mathbf{a}_p^n, \mathbf{F}_p^n = \sum_I \frac{\partial N_I}{\partial x_I^0} \cdot x_I^n \Delta F_p = \sum_I \frac{\partial N_I}{\partial x_I^n} \cdot x_I^{n+1}$

Initial data on nodes: NONE everything is discarded in the initialization phase

OUTPUT of calculation: $\mathbf{\Delta u}_p^n, \boldsymbol{\sigma}_p^{n+1}$

1. **INITIALIZATION PHASE**

   1.1 Clear nodal info and recover undeformed grid configuration
   1.2 Calculation of initial nodal conditions.
         (a) for $p = 1{:}N_p$
             Calculation of nodal data

$$\mathbf{q}_I^n = \sum_p N_I m_p \mathbf{v}_p^n$$

$$\mathbf{f}_I^n = \sum_p N_I m_p \mathbf{a}_p^n$$

$$m_I^n = \sum_p N_I m_p$$

(b) for $I = 1: N_I$

$$\widetilde{\mathbf{v}_I^n} = \frac{\mathbf{q}_I^n}{m_I^n}$$

$$\widetilde{\mathbf{a}_I^n} = \frac{\mathbf{f}_I^n}{m_I^n}$$

1.3 Newmark method: PREDICTOR. Evaluation of $^{it+1}\Delta\mathbf{u}_I^{n+1}$, $^{it+1}\mathbf{v}_I^{n+1}$ and $^{it+1}\mathbf{a}_I^{n+1}$ using Equations (73)-(75)

2. UL-FEM PHASE

2.1 for $p = 1: N_p$

(a) Evaluation of local residual (rhs) (Equation (43))
(b) Evaluation of local Jacobian matrix of residual (lhs) (Equation (57))
(c) Assemble rhs and lhs to the global vector RHS and global matrix LHS (Equations (61) and (68))

2.2 Solving system (Δu_I^{n+1})

2.3 Newmark method: CORRECTOR (Equations (74)–(76))
2.3 Check convergence
(a) NOT converged: go to Step 2
(b) Converged: go to Step 3

3. CONVECTIVE PHASE

3.1 Update the kinematics on the material points by means of an interpolation of nodal information (Equations (77)–(80))

3.2 Save the stress σ_p^{n+1}, strain ϵ_I^{n+1} and total deformation gradient $\mathbf{F}_p^{n+1}$ on material points (the latter by $\mathbf{F}_p^{n+1} = \Delta\mathbf{F_p} \cdot \mathbf{F}_p^n$)

3.5.2 Numerical difficulties

The use of linear basis functions within MPM has disadvantages. As stated in the introduction, the discontinuity of the basis function derivatives as well as the use of material points as integration points leads to numerical problems. In this section these problems are described in more detail.

GRID CROSSING

Within the original MPM, material points eventually cross the position where the derivative of a basis function is discontinuous. These so-called grid crossings influence the internal forces,

masses and external forces calculated at the degrees of freedom. To illustrate this effect at the hand of the internal forces, recall that the internal force at degree of freedom i is calculated in the following way:

$$F_{(t)}^{int,t} = \sum_{p=1}^{n_p} \sigma_p^t V_p^t \nabla \phi_t(x_p^t) \tag{82}$$

Figure 5 denotes a grid consisting of three degrees of freedom, in which four particles are defined. Assume each particle has the same stress σ and volume V, both constant over time. Furthermore, assume the derivative of the basis functions to be equal to -1 or 1. The internal force at degree of freedom 2 is then given by:

$$F_2^{int,t} = \sum_{p=1}^{n_p} \sigma V \nabla \phi(x_p^t) = 2\sigma V - 2\sigma V = 0 \tag{83}$$

Suppose one particle crosses x_2 where the derivative of the basis function associated to degree of freedom 2 is discontinuous. The internal force at degree of freedom 2 then suddenly becomes:

$$F_2^{int,t} = \sum_{p=1}^{n_p} \sigma V \nabla \phi(x_p^t) = \sigma V - 3\sigma V = -2\sigma V \tag{84}$$

Hence, grid crossing leads to a non-physical difference in the internal forces.
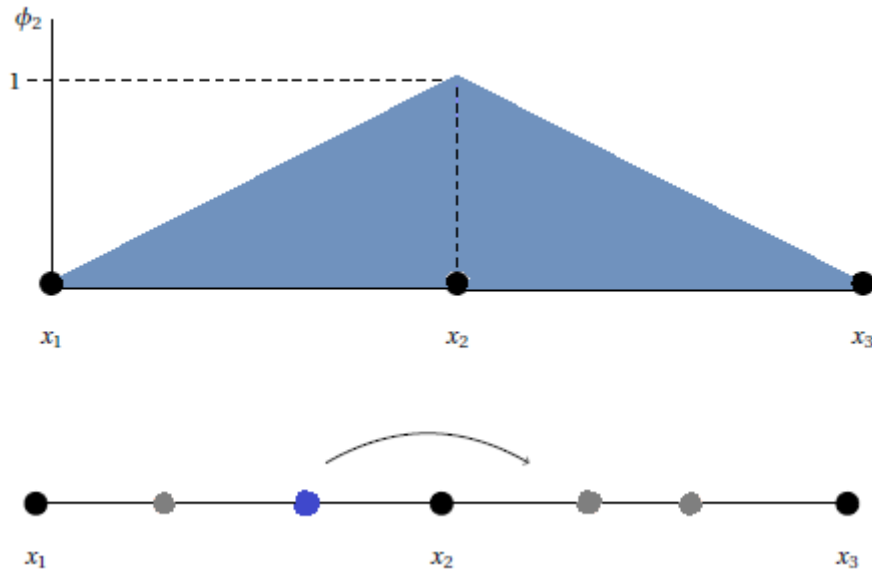
Figure 5: Illustration of grid crossing error [60].

To reduce the effect of grid crossings, Bardenhagen and Kober introduced in [3] a family of methods, named the Generalized Interpolation Material Point (GIMP) methods. The material point method can be seen as a special case of GIMP. While the effect of grid crossings was reduced, an increase of computational time was reported in [19].

In [1] and [7], stresses were determined at fixed Gauss points as the weighted average of particle stresses to reduce grid crossing errors. Other attempts to solve the problems associated with grid crossings were reported in [19], [24] and [66].

In [51] the spatial convergence of the material point method was determined when using different types of basis functions. Besides linear basis functions, both quadratic and cubic B-spline functions were used. When using linear basis functions, a lack of convergence was observed. Both quadratic and cubic B-spline functions showed spatial convergence up to a relatively high number of elements. Therefore, the use of higher-order B-spline basis functions was recommended [51].

QUADRATURE ERROR

In MPM integrals are approximated as follows:

$$\int_{\Omega t} f(x)dx \approx \sum_{p=1}^{n_p} V_p^t f\left(x_p^t\right) \tag{85}$$

Since material points move through the computational mesh over time, the position of the integration points changes every time step. The particle volume is used to approximate the domain over which integration is performed. This leads to a numerical integration rule of which the quality is uncertain. In general the numerical integration rule used in MPM is not exact.

The use of the particle volume as integration weight leads to a significant quadrature error when a discontinuous function is integrated. Note that within the MPM, the function $\nabla \phi_I$ is integrated to determine the internal force at the degrees of freedom. When Lagrangian linear basis functions are used, $\nabla \phi_I$ is discontinuous.

It was shown in some studies that the use of quadratic and cubic B-spline functions reduces this quadrature error. However, using the particles as integration points still leads to a numerical integration rule of which the quality is uncertain.

A solution to this problem might be the use of a numerical integration rule which uses integration points and weights at locations that render accurate integration. This approach is limited however by the fact that physical properties like density and stress are only known at the particle positions. The values of these quantities at integration points have to be approximated from particle data. To do this more elaborately, function reconstruction techniques can be used. With this approach a function is reconstructed based on a finite number of known function values. To obtain an approximation of the quantity of interest at the integration point, the function can be evaluated at this position.

In [22], a weighted least squares approach was used to reconstruct, among other quantities, the density field from the known values at the particle positions. After reconstructing the density field, a one-point Gauss rule was used to approximate the integrals. To reduce the numerical quadrature error (cubic) spline interpolation would be used as a function reconstruction techniqu

4. Numerical examples

4.1 Validation of the method

In this first section of the numerical analysis the objective is to validate the Material Point Method. For this approach, a series of standardized tests on concrete samples were carried out using damage models. The reason to perform these tests is because they are standardized tests, which means that the experimental behaviour is known. They are also easy to simulate and compare with the classical finite element method, FEM.

Furthermore, through these analyses, it can be accurately observed if the method calculates correctly the different stresses to which the structure can be subjected (compression, tension and shear).

On the other hand, the use of damage models allows to simulate the collapse of the material and see if the fracture mode is as expected, considering the softening of the material by deformation through a surface of damage.

4.1.1 Compression test

4.1.1.1 Two- dimensional analysis
To carry out the analysis, it is considered that a much more resistant material than concrete (for example steel) acts on the upper part of the specimen, simulating this analysis.
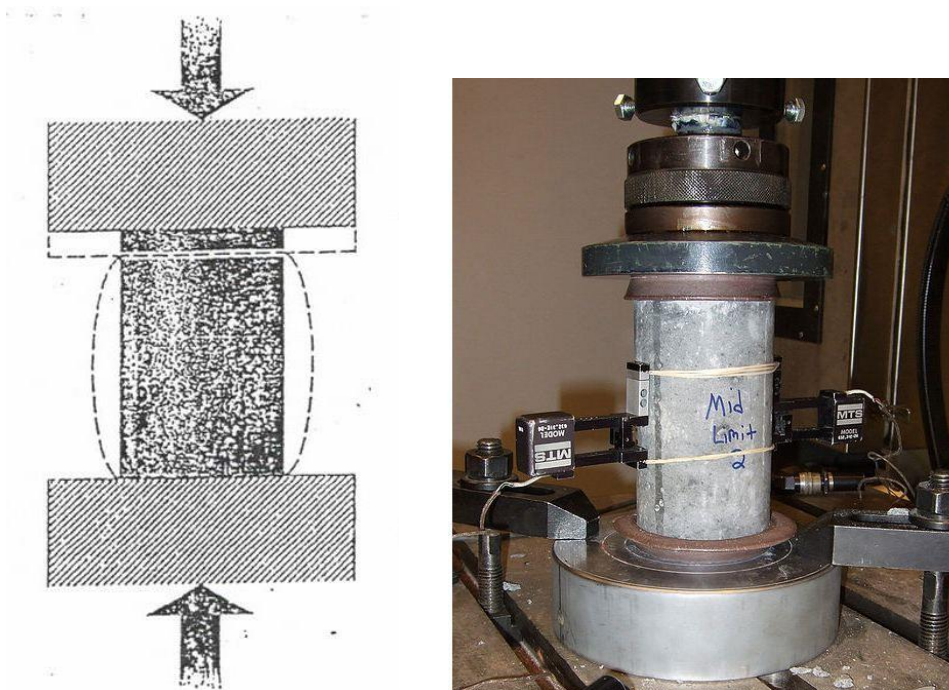
Figure 6: Methodology of the compression test [64].

Some analysis tests have been carried out. For this, a concrete test tube with the following properties and dimensions is used:

Description of the geometry and properties of the material.

Material properties

	Concrete sample	Steel plate
Density (Kg/m3)	2410	7870
Young Modulus, E (kg/ms2)	3,55E+10	2,00E+13
Poisson ratio	0,2	0,29
Thickness (m)	1	1
Yield Stress	3,00E+05	
Damage threshold	16,187719	
Strength ratio	1,23E+01	
Fracture energy (J o N·m)	100	

Table 1: Materials properties.

Geometry of the model
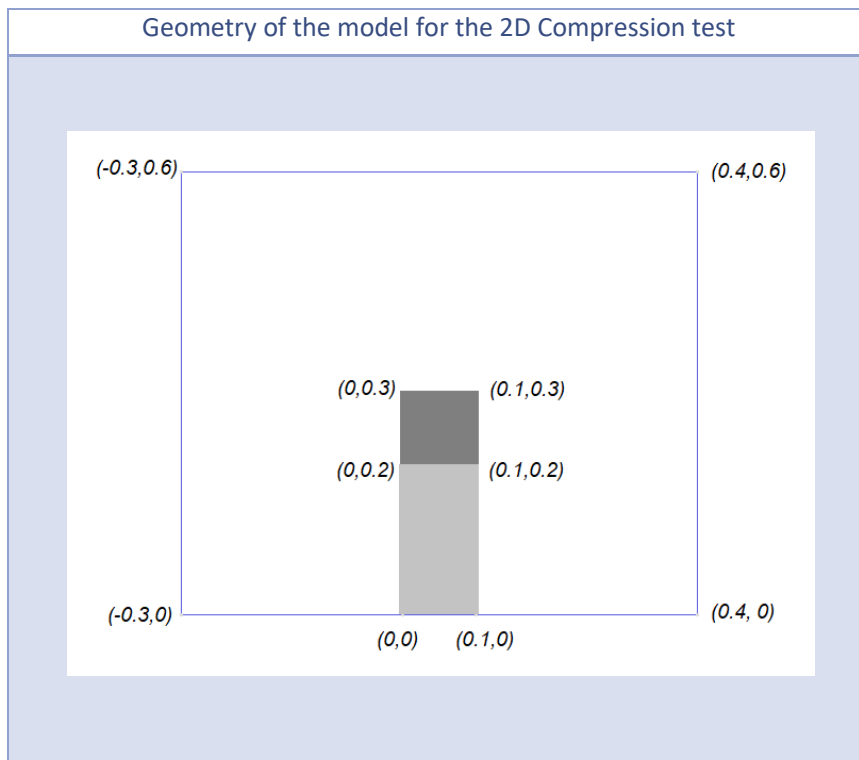
Image 1: Dimensions of the sample and the background mesh for the 2D test.

In order to see how the method behaved, several analyses have been carried out with different types of mesh, different displacements imposed by step, etc. This is detailed in the following table:

Types of meshes for the analysis

Mesh type		Unstructured sample size	Structured sample size	Background mesh size
Triangular	T1	0,0075	0,0075	0.00648148
Triangular	T2	0,005	0,005	0.00648148
Triangular	T3	0,0025	0,0025	0.00648148
Quadrilateral	Q1	-	0,0075	0.00648148
Quadrilateral	Q2	-	0,0065	0.00648148
Quadrilateral	Q3	-	0,005	0.00648148

Table 2: Analysis performed for the compression test.

Mesh type	Background mesh size	Mesh size	Displacement	Steps	Nº particles
Q1	0.00648148	0,0075	-1,00E-06	300	2
Q2	0.00648148	0,0065	-1,00E-07	2000	2
Q3	0.00648148	0,005	-2,00E-06	300	2

Table 3: Analysis performed with quadrilateral meshes.

Stress-strain curves for 2D cases.

Several analyses were carried out with meshes of triangular elements (see Table 2) but these did not show sufficiently good results. It was thought that perhaps with meshes of quadrilateral elements would be improved since the geometry is rectangular and maybe the mesh responds better.

After performing several analyses with quadrilateral meshes, it was observed that the results were much better. Within the analyses with quadrilateral meshes the better results are obtained with the one that has the finest mesh and a displacement by step a little bigger (Case Q3).

This makes sense because having a finer mesh in the sample means having more material points and therefore the solution is closer to reality, therefore it is an expected result and we consider it good. Below, the stress-strain curves obtained in our analyses are shown and compared with experimental laboratory curves.
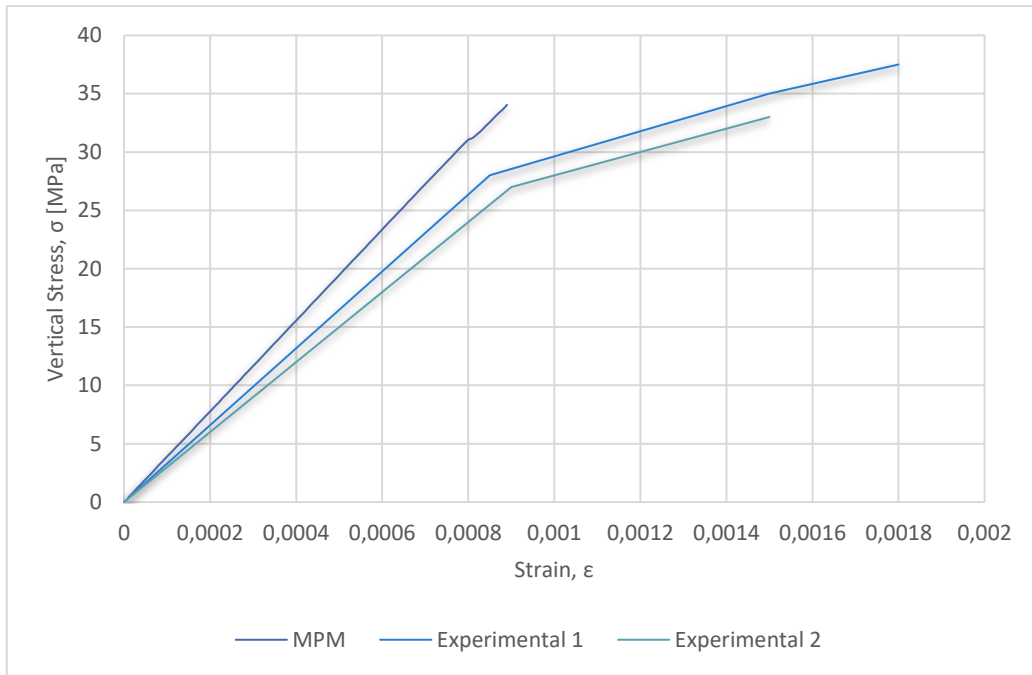
Graph 1: MPM Q3 and Experimental strain-stress curves for two-dimensional analysis.

In this first graph, the stress-strain relationship obtained for the test that gives the best results (Q3) is shown. As can be seen, our material behaves in a more rigid way than in the experimental case, that is, the MPM sample is deformed much less for the same stress, compared to the laboratory.

Here could be seen the curves get for the others test Q1 and Q2:
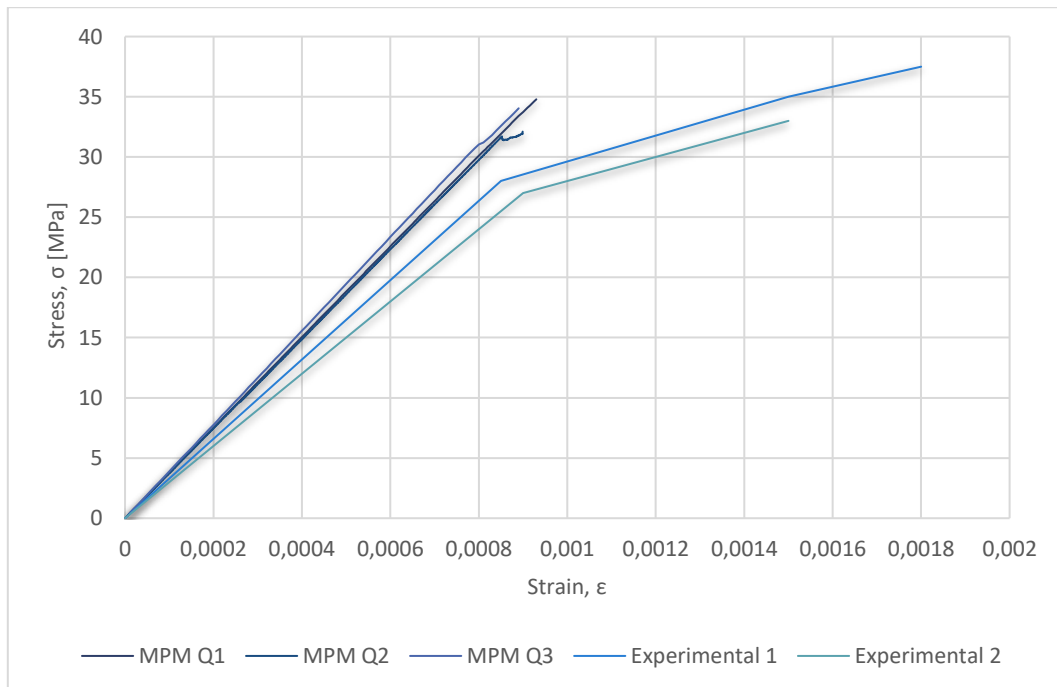
Graph 2: Stress-strain curve for MPM 2D Compression and experimental analysis.

It can be seen that between the results with the different performed MPM tests practically the same curves are obtained, which makes sense. Note that after the analysis we decided that the case Q3 was the one that gave better results because it was the one that reached a damage equal to 1, also its damage distribution and its way of fracture (its fracture surface) was like the experimental. In the next figures these results are shown.

Main results for 2D cases

Damage distributions
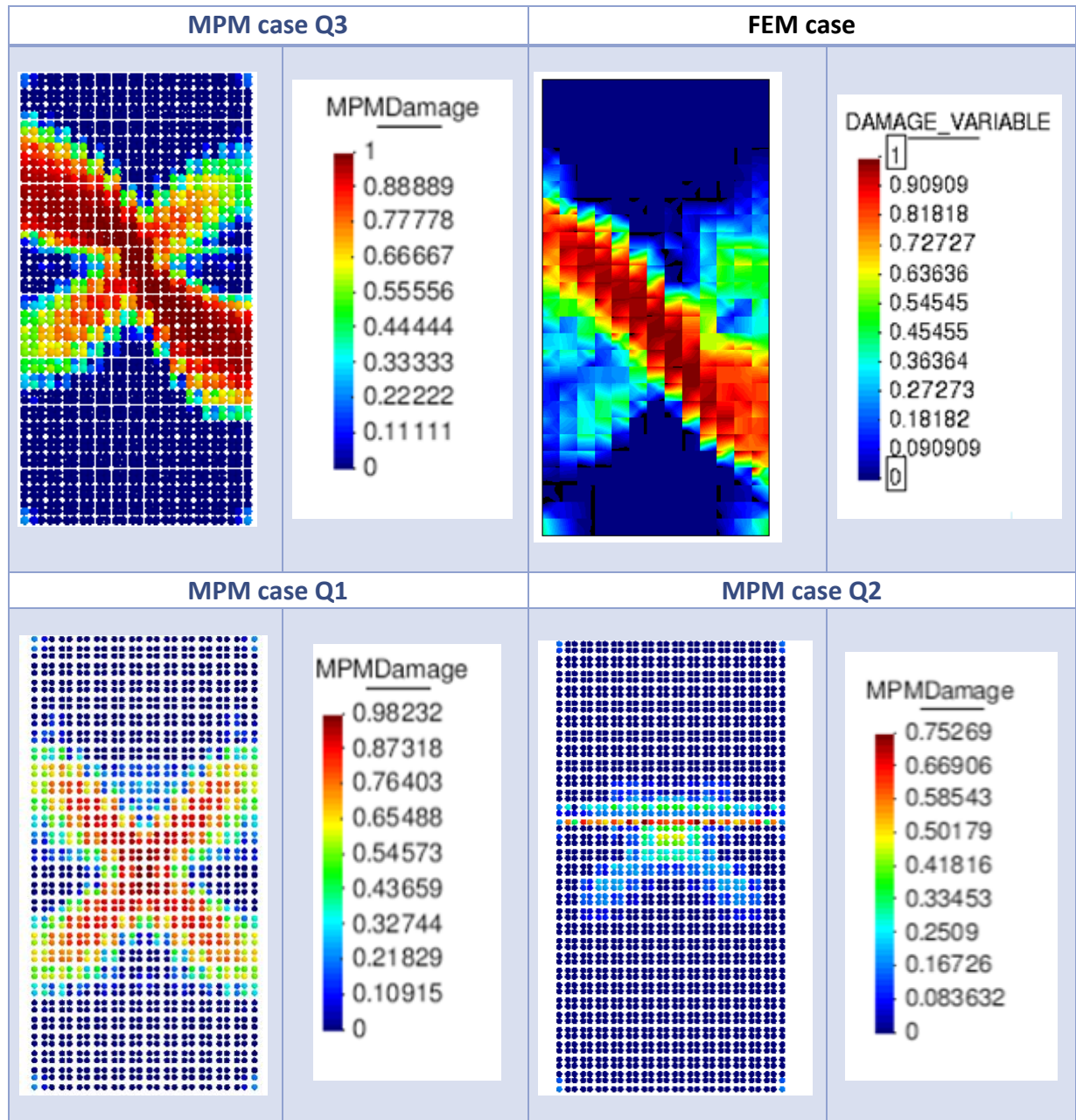
<div align="center">Figure 7: MPM and FEM damage distributions.</div>

As can be seen in the damage results, the case that gives better results is Q3. The comparison with FEM has been made and it can be seen that clearly the break occurs in the same way. So, it could be seen that the method works correctly.

As I said the test tube reaches a damage equal to 1, which means that it breaks. In addition, damage occurs in the form of a cross, as expected, since in this way occurs in experimental tests. And on the other hand, the fracture surface occurs diagonally and is practically the same as that obtained with FEM. So, it is understood that the MPM in a 2D compression test is validated.

The main aspect in which the Material Point Method does not calculate the results too well is in the stresses.

It can also be observed that the fracture surface that is obtained is conditioned by the mesh of the specimen, this is an aspect by which the code should be modified to improve the results in the future work.

In the following figures, the stress distribution obtained for the case Q3 is shown and compared with FEM.
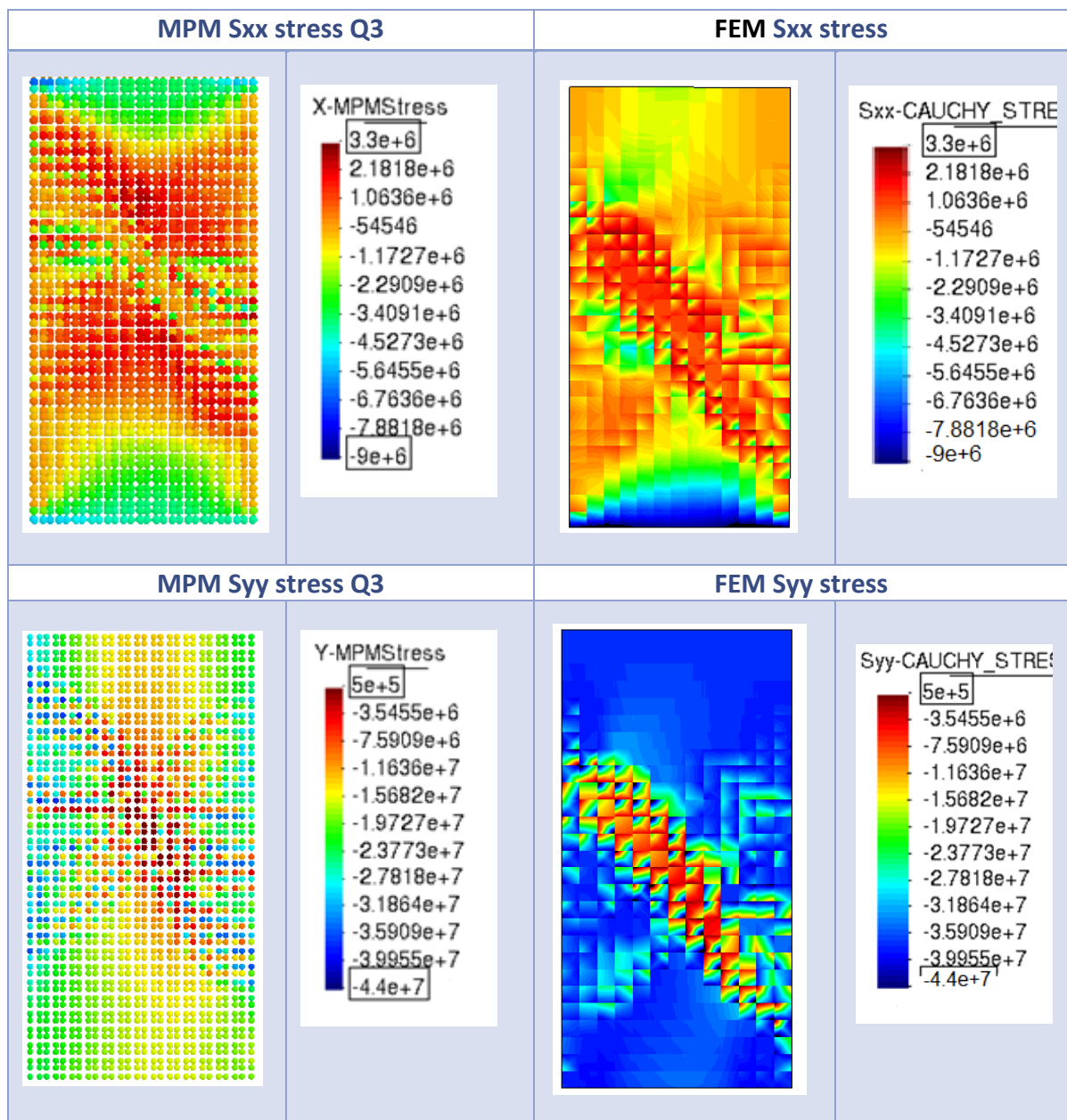
Figure 8: MPM and FEM stresses.

In FEM it can be seen that the stresses are a little more defined than with MPM. Even so it can be observed that the stresses that are obtained in the fracture surface are similar. As future work it would be necessary to improve the calculation of the stress in the method.

4.1.1.2 Three-dimensional analysis

On the other hand, different simulations of the 3D compression test have also been carried out. It is expected that, as it is a three-dimensional analysis, the results will be better and more realistic. In this section the best results obtained for 3D are shown. The parameters used for the analysis are:

Mesh size	Background	0.018
	Sample	0.017
Imposed displacement		-1,00E-06
Nº particles		4
Nº steps		193

Table 4: Characteristics of the three-dimensional analysis for a compression test.

Description of the geometry and properties of the material.

In the three-dimensional case, a cylindrical sample is considered, the material properties are the same as for the two-dimensional case and the geometry is shown below

Geometry of the model for the 3D Compression test

(-0.05,0.25)　(0.05,0.25)

(-0.05,0.2)　(0.05,0.2)

(-0.05, 0)　(0.05,0)
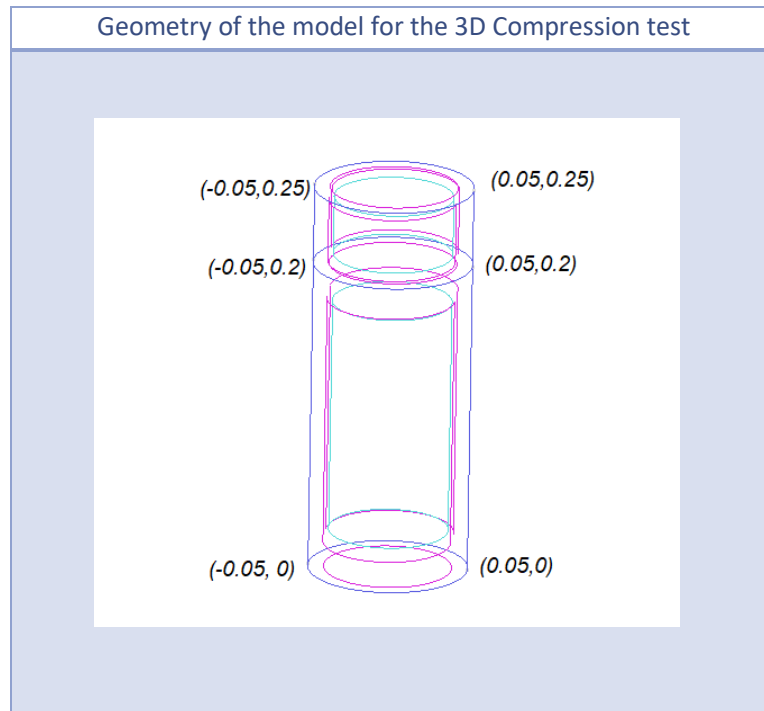
Image 2: Dimensions of the sample for the 3D test.

Note: The background mesh is a hexahedron with vertices: (0.07, 0, 0), (0, 0, -0.07), (-0.07, 0, 0), (0, 0, 0.07), (0.07, 0.3, 0), (0, 0.3, -0. 7), (-0.07, 0.3, 0) and (0, 0.3, 0.07).

Stress-strain curves

To validate the model, it has been verified which was the stress-strain relationship that the test sample experiences. This curve has been compared with several experimental curves for this type of concrete.
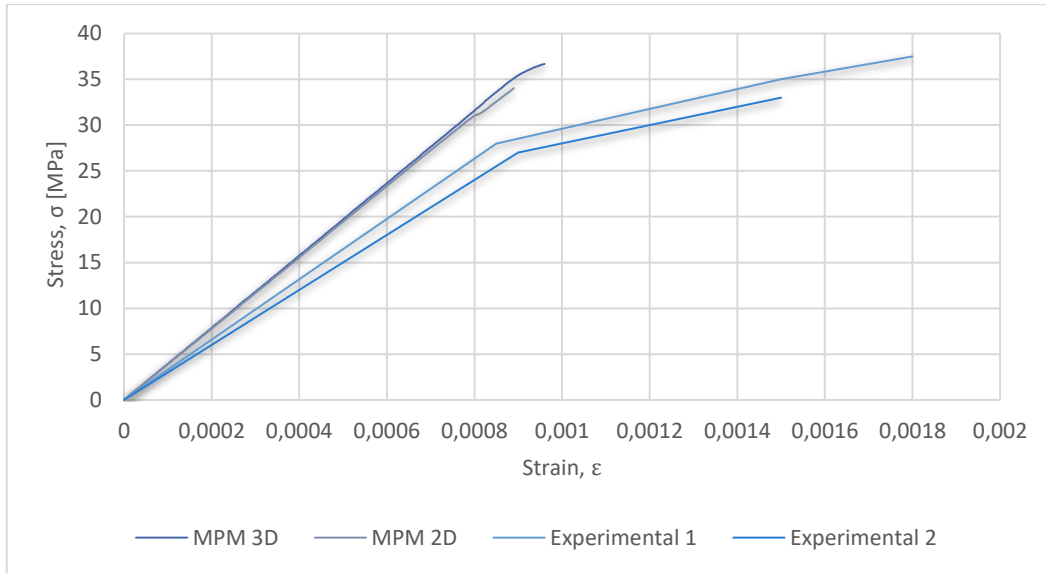
Graph 3: MPM (2D and 3D) and Experimental stress-strain curves.

It is observed that the result obtained in 3D is similar to that obtained in 2D. The stress-strain curves of the MPM for both cases have practically the same slope, reaching the expected resistance limits. However, with the MPM, the material continues having a more rigid behaviour, as in two dimensions for the same stress value, the sample deforms less in MPM than in the experimental results.

Main results for 3D cases
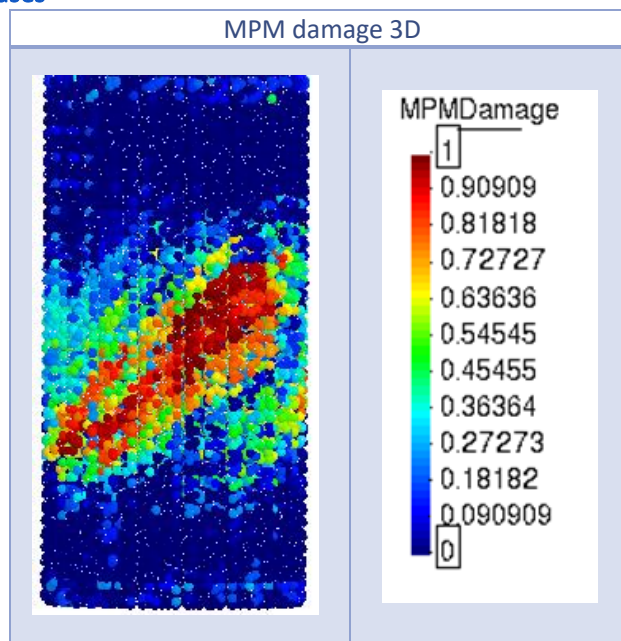
Figure 9: MPM 3D final damage distribution.

In the previous figure it is shown that the distribution of damage is what was expected, a good 3D analysis is obtained, and the concrete fractures (damage equal to 1). However, it is shown below that the stresses do not give the best results.

MPM case Q3	FEM case
MPM case Q1	MPM case Q2
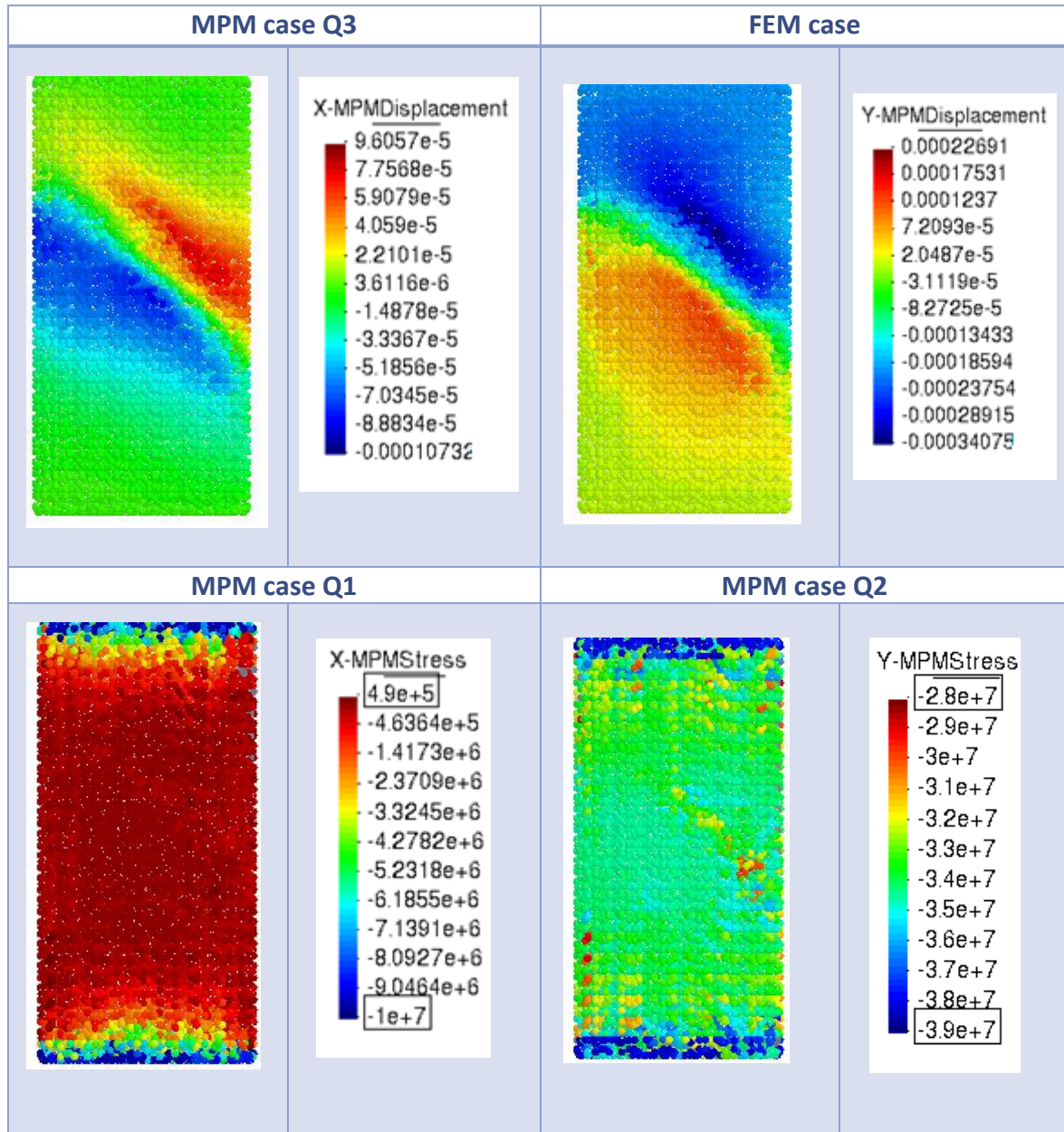
Figure 10: MPM 3D displacements and stresses.

The sample moves as expected and in the two upper figures of the previous table it can be observed. While in the lower part it is shown that the tensions acquire an ill-defined distribution, the cross of stresses is not shown as can be seen in 2D or of course in FEM.

The results of the stresses are therefore a bit worse in 3D and it will be necessary to investigate this behaviour and how to improve it for future work.

Figure 11: Experimental fracture for concrete samples [64].

Figure 11 shows the fracture of the test piece in laboratory. This fracture is similar to the one obtained in the simulations, part of the concrete is detached from the specimen as the tension increases on it. The fracture occurs diagonally, behaviour that also occurs in numerical simulations with MPM.

It is necessary to emphasize that the failure result computed by the method is a numerical fracture, that is, the method considers that the material fails when one of the material points reaches a very large displacement that makes it protrude from the element. Therefore as a future line of research it is necessary to make different modifications on the code in order to solve this problem.

4.1.2 Brasilian test

Tensile strength of concrete is among the most important parameters influencing its deformability. To calculate the tensile strength an indirect tensile (Brazilian) test is performed.

In this test we have a cylindrical concrete sample (positioned as shown in the following figures), on this specimen a metallic material applies a displacement downwards. In this way we analyze what is the maximum stress that concrete has and how it breaks. Below a table with the properties of the materials used for the concrete sample and the steel plate is shown.

	Concrete sample	Steel plate
Density (Kg/m3)	2410	7870
Young Modulus, E (kg/ms2)	3,55E+10	2,00E+13
Poisson ratio	0,2	0,29
Thickness (m)	1	1
Yield Stress	3,00E+05	
Damage threshold	16,187719	
Strength ratio	1,23E+01	
Fracture energy (J o N·m)	100	

Table 5: Material properties of the Brazilian test.

As we intend to validate the model, we expect our numerical fracture with MPM to be similar to that produced in experimental laboratory tests. Below are images of this test in laboratory.

Figure 12: Methodology and fracture of experimental sample in a brasilian test [18].

4.1.2.1 Two-dimensional analysis

First several 2D simulations have been made. In the beginning, the geometry of the model is described as well as the characteristics of the tests. The results obtained for different evaluated trials are shown below.

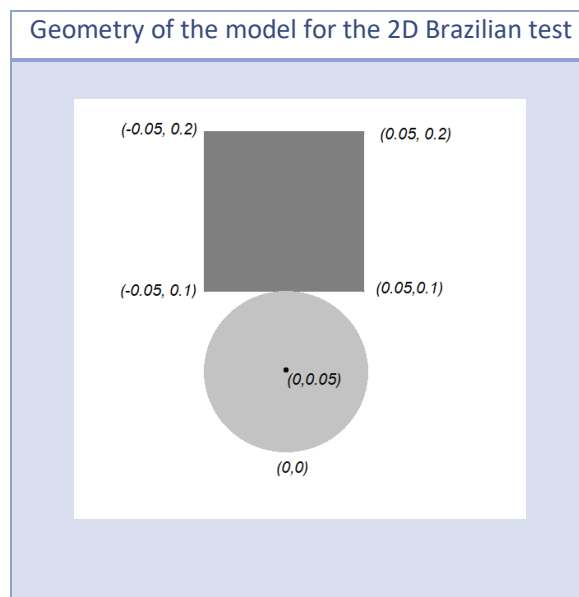**Description of the geometry and properties of the material.**

Geometry of the model for the 2D Brazilian test

(-0.05, 0.2)   (0.05, 0.2)

(-0.05, 0.1)   (0.05,0.1)

(0,0.05)

(0,0)

Figure 13: Geometry of the concrete sample and the steel material imposing a displacement.

To obtain a good analysis of the Brazilian test with MPM, different tests have been carried out. In these tests have been modified the size of the meshes, times, the number of particles and the displacement for step, to see how the method reacts.

In this table the characteristics of the tests are shown:

Mesh type	Mesh size (triangular mesh)	Background mesh size	Displacement/step	Nº steps	Nº Particles
Case 1	0,005	0.005	-1,00E-06	1000	3
Case 2	0,005	0.005	-2,00E-06	1000	3
Case 3	0,005	0.005	-5,00E-07	1200	3
Case 4	0,005	0.005	-1,00E-06	1000	6

Table 6: 2D analysis performed for a brazilian test.

The best results have been obtained for case 1 and case 4, in case 4 a higher number of particles have been used to see if the solution improves. This analysis has been compared with one of equal dimensions and characteristics using FEM to see if the method works.

In the Brazilian test, the specimen breaks through the tensile stress limit (Horizontal stress, S_{xx}). The curves obtained from the analysis are shown below, although it should be noted that the curve by which the concrete sample breaks is that of the horizontal stress, S_{xx})., when the limit is reached, in our case 3.5 MPa.

Vertical stress until damage occurs in the specimen (numerical fracture)

Stress-strain curves for 2D cases
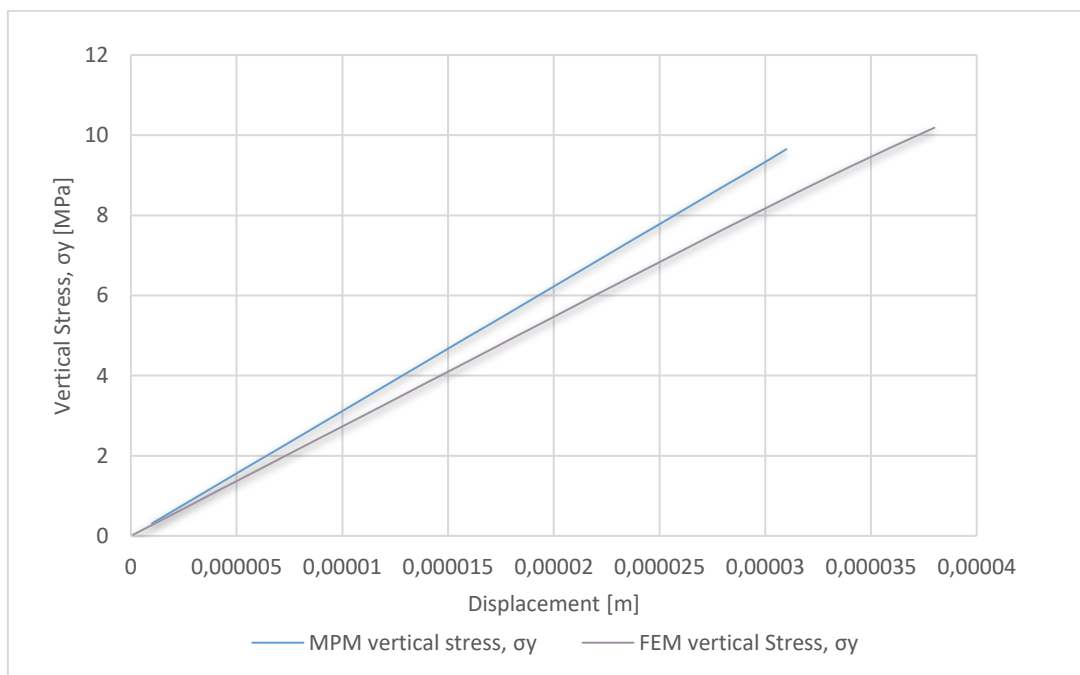
Graph 4: 2D vertical MPM and FEM strain-stress curves for a Brazilian test.

In the previous graph you can see the vertical stress that occurs in the concrete sample analysis in MPM and FEM. The behaviour is similar for both methods, the slope is also similar but as it happened with the compression test in this case the material is also more rigid and deformes less in MPM for the same vertical stress compared with FEM.

However, in spite of this graph in which the relation between displacement and vertical stress is shown, the graph that gives us information on whether the method calculates correctly is that of horizontal stress as a function of displacement or deformation, given that the specimen breaks by indirect traction, that is to say the horizontal stress S_{xx} reaches the limit value of the traction for concrete.

Horizontal stress until damage equal to 1 occurs in the sample. When the S_{xx} reaches the limit, damage variable is equal to 1 and the sample breaks. (fracture).
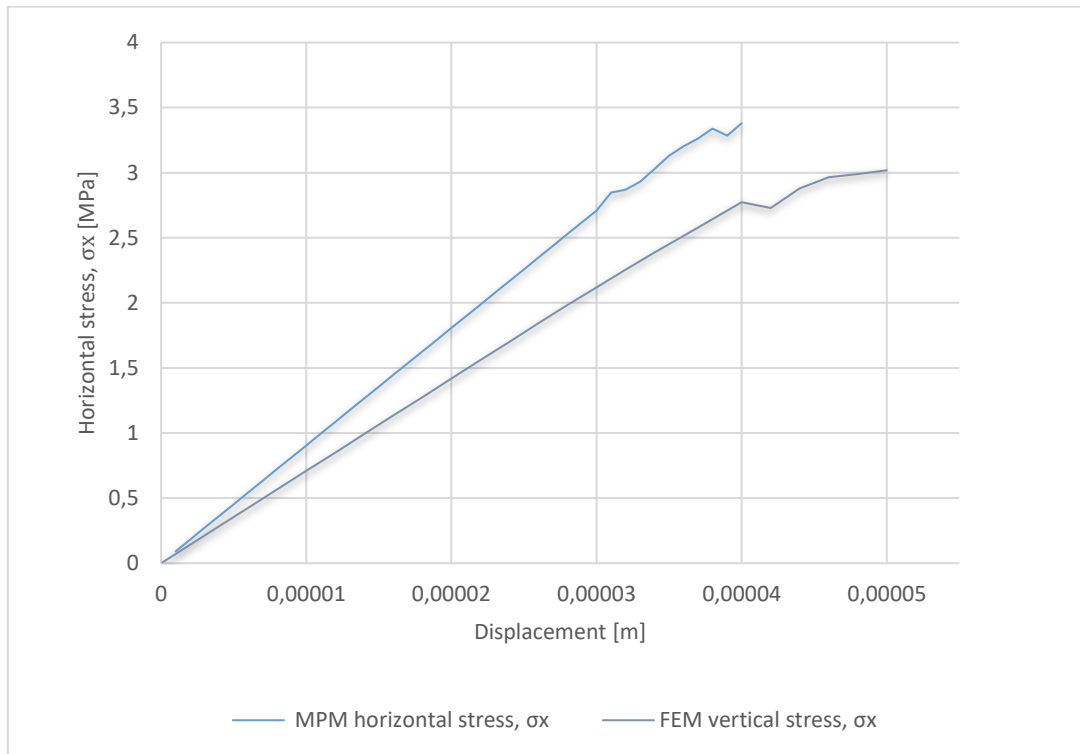
Graph 5: 2D horizontal MPM and FEM strain-stress curves for a Brazilian test.

As can be seen in Graph 4, the stress-displacement curve obtained is as expected, it is shown that the fracture of the sample occurs when the concrete reaches its tensile limit, that is, for a stress of 3.5 MPa.

Below, are shown some damage distributions obtained for some of the analyses performed. It is also shown the results obtained using a higher number of particles. All distributions are compared to FEM, as well as stress-strain curves (see Graph 5).

Damage distributions for different cases
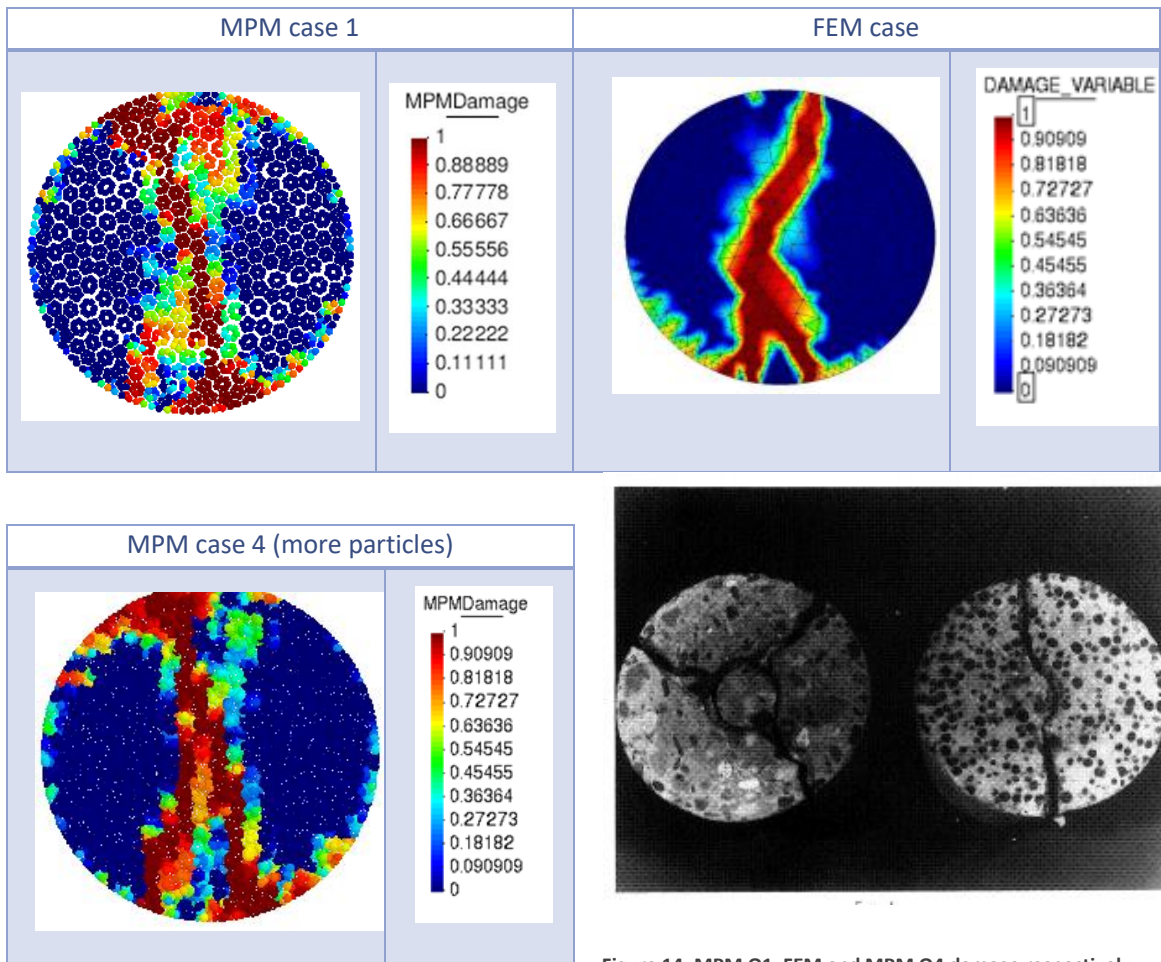
Figure 14: MPM Q1, FEM and MPM Q4 damage respectively.

It can be seen that the fracture mode is similar to that produced in the laboratory test tubes and also similar to FEM. When the number of particles is increased, the solution with MPM approaches that obtained with finite elements. This makes sense given that a higher number of particles means that in the simulation the stresses are calculated in a higher number of nodes, which causes a solution closer to the real, as happens if the mesh size is reduced. The solution is always more accurate and closer to the real one when the size of the mesh is smaller (finer mesh) and when we have a greater number of particles. Despite this, in the compression analysis, the results were considered good enough to increase the number of particles, since it is necessary to take into account that a greater number of particles implies a longer calculation time of the simulation.

The following shows how the test piece moves in the analysis, the displacement makes sense since the test piece breaks and each one of the halves moves to one side.
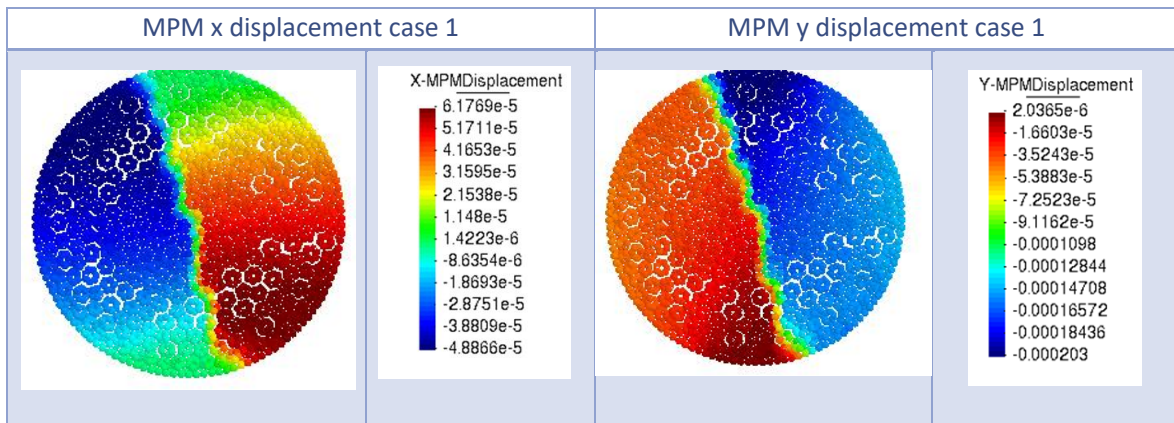
Figure 15: 2D MPM horizontal and vertical displacements.

On the other hand, the results obtained for the stresses are analysed, which, as it has been mentioned previously, is the most critical point of the method. The horizontal stress that occurs in the sample is of the order that occurs with the finite element method although it may be a bit smaller. For the case in which there is a higher number of particles it can be seen that the stress in MPM is a little lower in the centre of the concrete sample, than that obtained with FEM.

Regarding the vertical stress, in this case better results are obtained. The distribution of stresses is much more defined mainly at the breaking surface. Comparing it with FEM it can be seen that the stress reached is the same and that for a larger number of particles the calculation is even more accurate (see Figure 17).
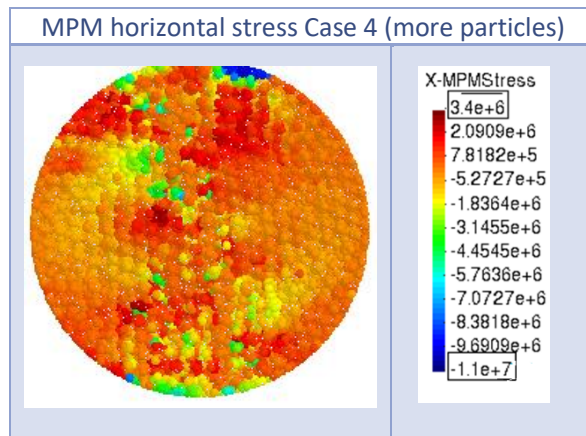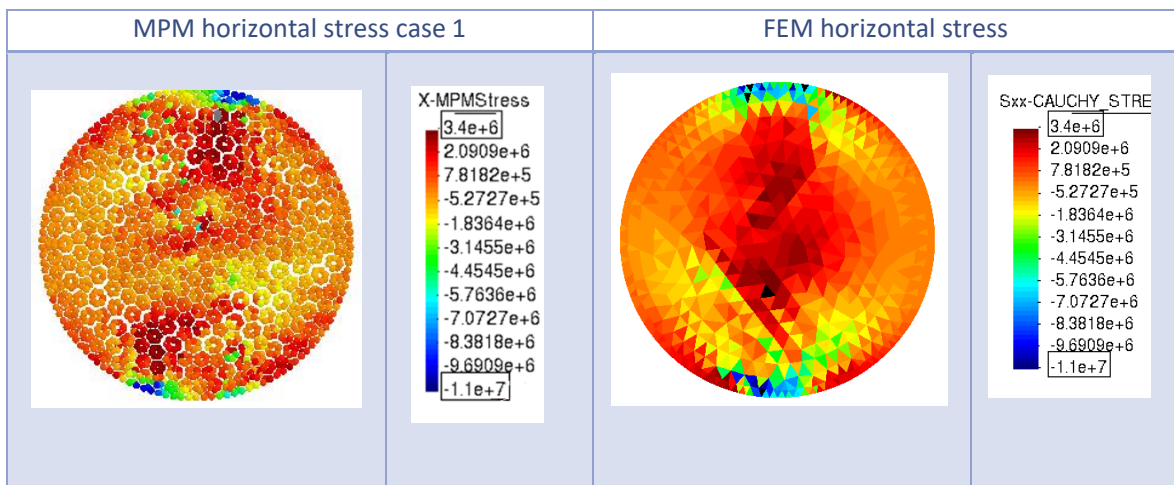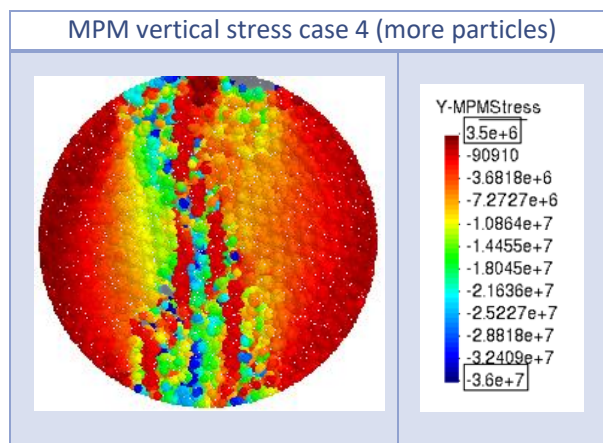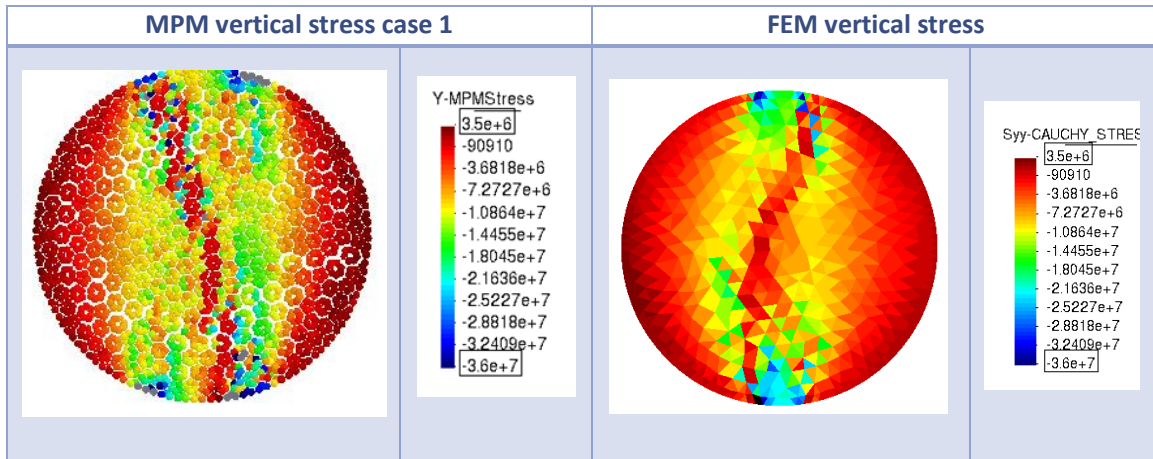

Figure 17: MPM Q1, FEM and MPM Q4 vertical stress respectively.

4.1.2.2 Three-dimensional analysis

Later, a 3D analysis was carried out to see if it could improve the results obtained in 2D, since it is a more real analysis. The characteristics of the test are the following:

Mesh size	Background	0.017
	Sample	0.007
Imposed displacement		-1,00E-06
Nº particles		4
Nº steps		193

Table 7: Characteristics of the 3D MPM analysis for a Brazilian test.

Stress-strain curves for 3D cases

The stress-strain curves for the 2D, 3D and FEM analyses have been compared in a graph.
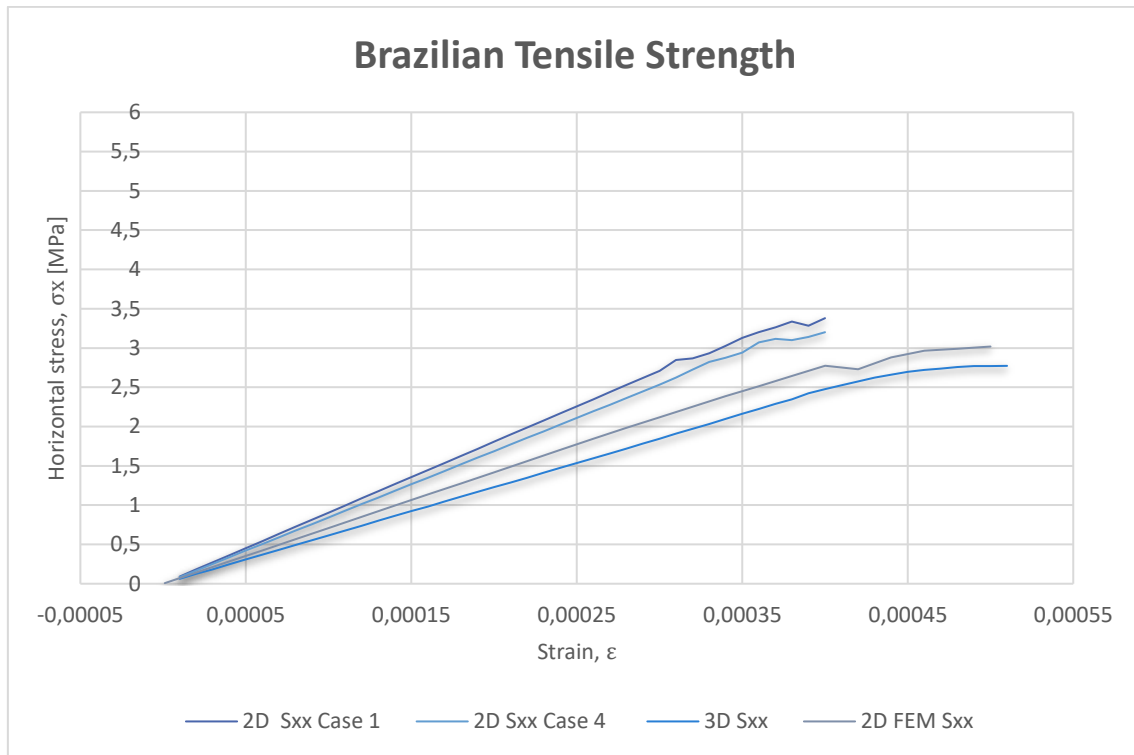
Graph 6: MPM (2D and 3D) and FEM stress-strain curves in a Brazilian test.

As can be seen, the method improves and approaches the FEM solution if we use a greater number of particles, or even more if we perform the analysis in 3D. This makes a lot of sense and is expected, because having a larger number of particles the analysis is more accurate. And 3D analysis is more realistic, so the solution is closer to that of FEM.

Main results for 3D cases

After performing the indirect traction test in two dimensions, it has been processed to perform it in 3D to see if better results are obtained. Next, one of the damage distributions that has been obtained for this case is exposed.
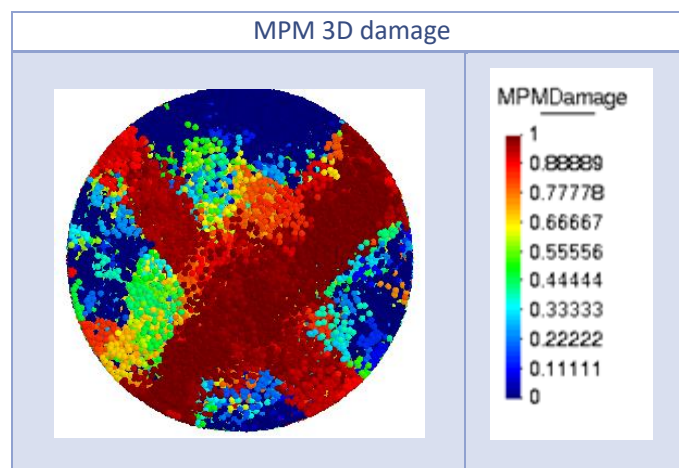

Figure 18: 3D MPM damage distribution in a Brazilian test.

It can be observed that the way in which the test piece breaks is expected, the concrete reaches the maximum tensile stress and therefore reaches a damage value equal to 1 and breaks. Once again, a cross-shaped fracture is generated that causes the material to split.

As shown in Graph 6, the stress strain curve obtained in three dimensions is more accurate and closer to FEM, that is, the results improve for the 3D case.

The displacements and stresses that occur in the concrete specimen for the 3D test are shown in the figures that follow. The displacements are the expected ones while the distributions of horizontal tensions are a little lower than in the 2D case and also less defined in the fracture surface.
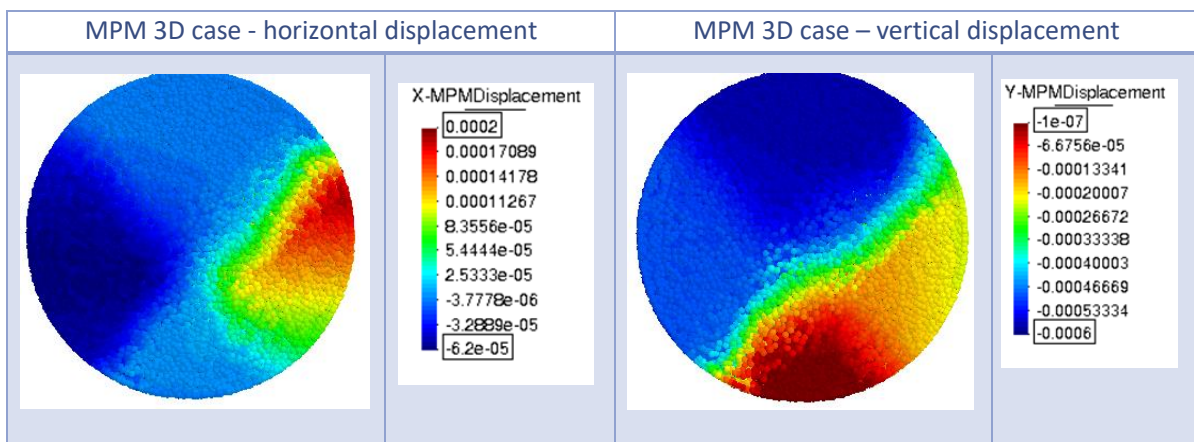

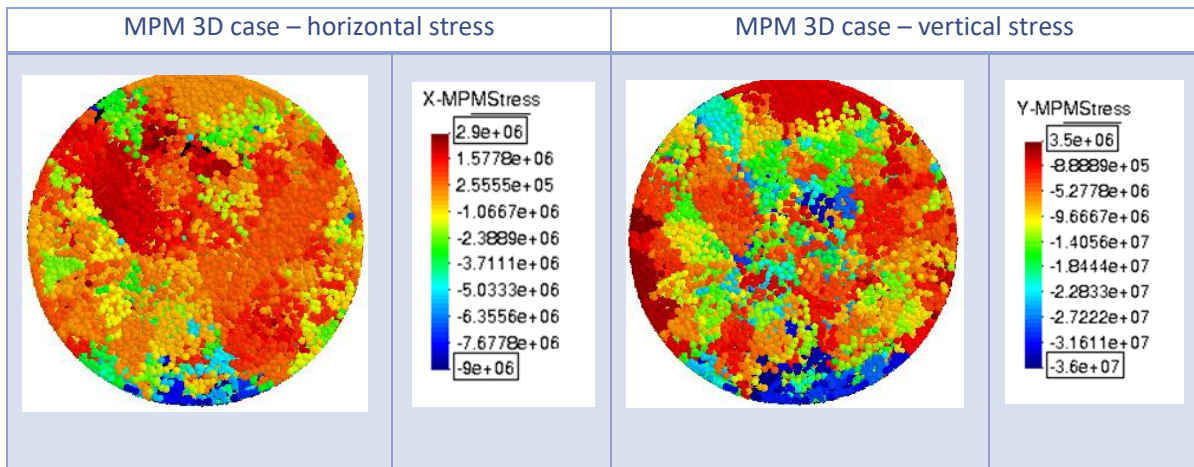Figure 19: 3D MPM horizontal and vertical displacement.

Figure 20: 3D MPM horizontal and vertical stresses distribution.

The vertical tensions reach the values obtained in FEM and in this same analysis in 2D, although they are more dispersed and less concentrated near the fracture surface. The distribution of tensions is a point of the MPM that must be improved especially in the three-dimensional case, since as shown the results are not precise or defined.

4.1.3 Shear test

On the other hand, a shear analysis has been carried out. In this analysis, a concrete sample is subjected to a series of shear forces (simulated by displacements in this case). In Figure 21 is shown the test configuration.
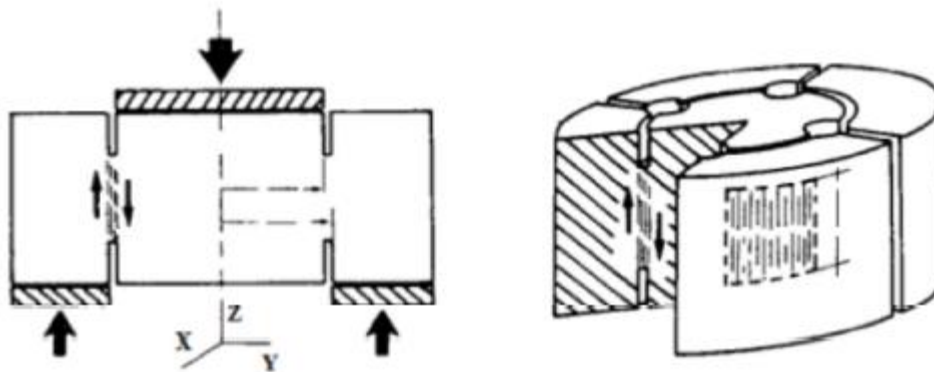

Figure 21: Configuration of the shear test [18].

4.1.3.1 Two-dimensional analysis

For this test, only a 2D analysis has been carried out because it already offered quite good results. The following figures show the geometry and properties of the materials used for the simulations.

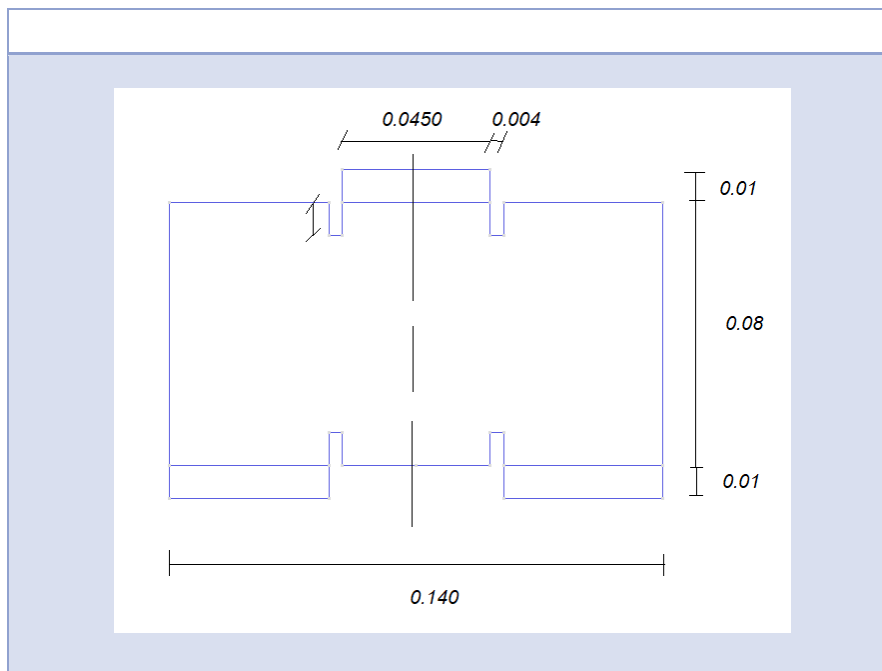**Description of the geometry and properties of the material.**

Figure 22:Dimensions of the concrete sample in the Shear test.

	Concrete sample	Steel plate
Density (Kg/m3)	2410	7870
Young Modulus, E (kg/ms2)	3,55E+10	2,00E+13
Poisson ratio	0,2	0,29
Thickness (m)	1	1
Yield Stress	3,00E+05	
Damage threshold	16,187719	
Strength ratio	1,23E+01	
Fracture energy (J o N·m)	100	

Table 8: Properties of the materials.

Initial time	0
Time step	1
Final time	300

Table 9: Times for the analysis.

Main results for 2D cases

As can be seen, the damage distribution obtained is the expected one since the test piece breaks through the weakest part (which is subjected to pure shear). Damage equal to 1 is attained (In red in Figure 23) which means the fracture of the specimen.
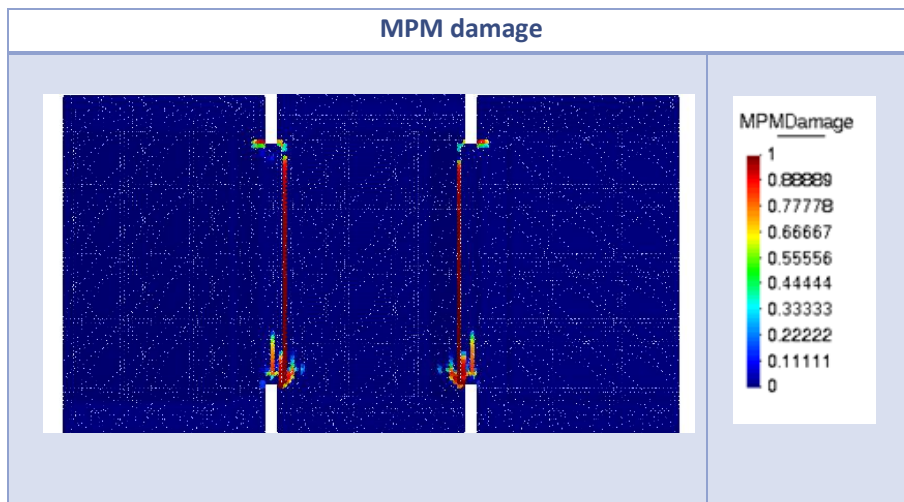

Figure 23: 2D MPM damage distribution shear test.

The displacements and stresses that occur in the specimen for this test are also shown.
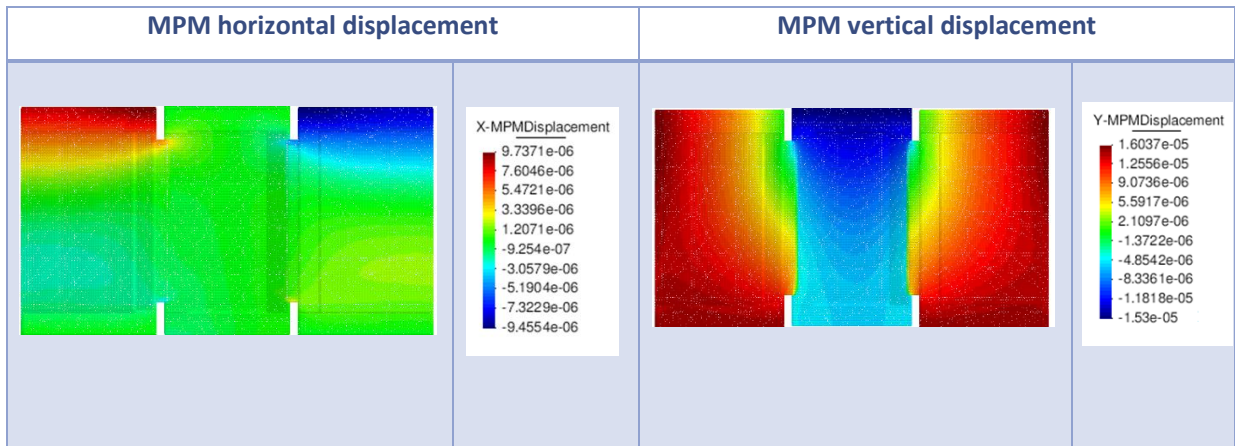
MPM horizontal displacement	MPM vertical displacement

Figure 24: 2D MPM horizontal and vertical displacement Shear test.

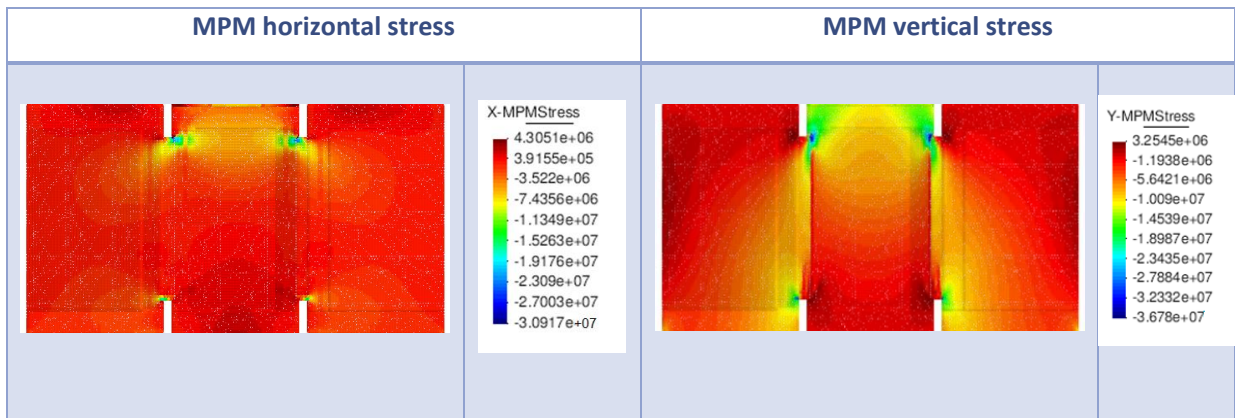| MPM horizontal stress	MPM vertical stress

Figure 25: 2D MPM horizontal and vertical stress Shear test.

The distribution of stresses that is obtained is more defined than in the other two tests. It can be seen that a stress concentration occurs (in blue colour in Figure 25) in the critical areas of the sample (where the fracture crack begins to be generated).
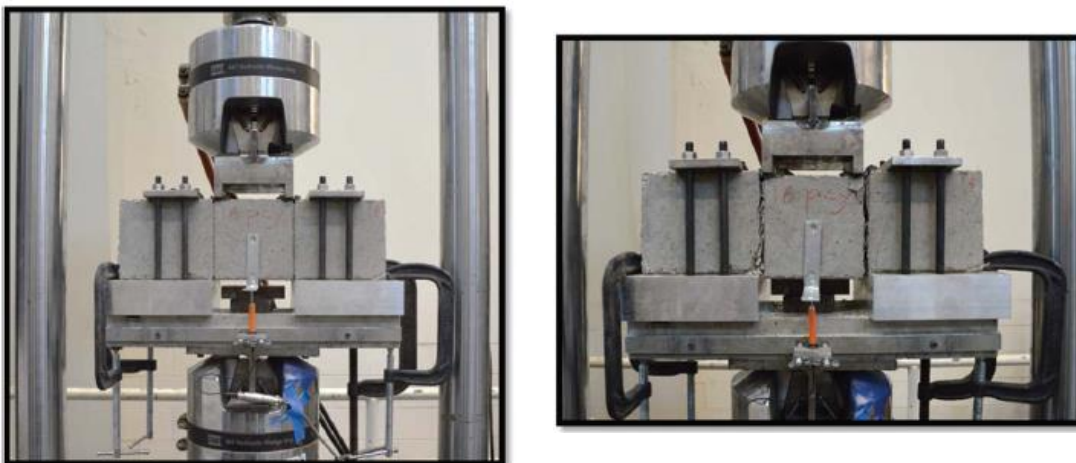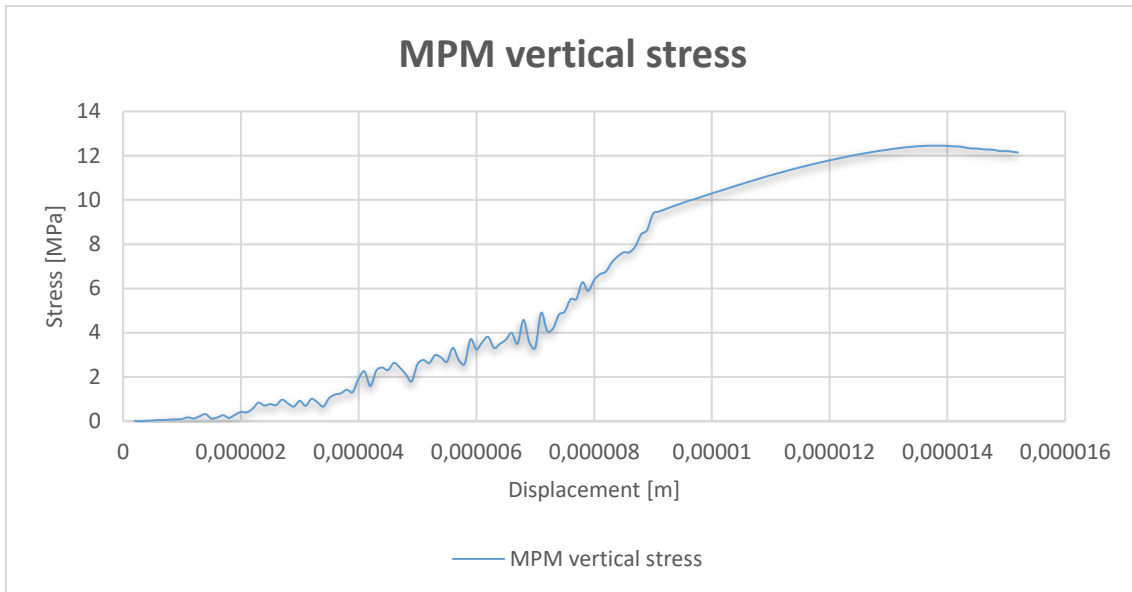

Figure 26: Test setup and way of fracture for direct shear test [40].

On the other hand, it is interesting to analyse what was the relationship between the tension and the displacement that occurred in the numerical simulations. Next, the vertical tension-displacement curve.

Graph 7: Stress-displacement curve for the 2D MPM Shear test.

It is observed that as the pistons exert a displacement on the sample, the stress is increased, and with it the deformation of the sample. A maximum displacement of 1.4E-5 m is reached for a maximum stress of approximately 12.5 MPa.

Figure 27: Fractured experimental samples for a H30 concrete in a shear test. [11]

In the previous image it is shown that the test pieces in the laboratory break in the same way as in the analyses.

4.2 Preliminary MPM dam's fracture analysis.

Since the MPM is a good method when large deformations occur in external conditions. It is interesting to use it in dams, as future work is intended to break the dam's core in extreme conditions. For now, the results obtained are not good but as first approximations can be useful when it comes to see how the structure behaves.

For the analysis of the dam, the Mohr-Coulomb break criterion was used, although others such as the Drucker Prager model could also be used.

The objective is to simulate the impact of water on the dam's coronation, using volumetric forces. Results have been obtained in 2D in which the core fracture is shown

As it is simulated in extreme conditions, it has been considered that the rockfill of the shoulder and coronation has already been dragged by the water, leaving the semi-discovered core as shown. The geometry and the properties used are shown below.

Note that it is shown the preliminary analyses that have been carried out to simulate the fracture of a dam. The goal is to simulate future fracture of the dam's core in extreme conditions with reliable results. For now only preliminary analyses are available, in which it is aware that there is a lot of work ahead. The analyses have been carried out applying volumetric loads on the structure. With these volumetric loads it is intended to simulate the push of water on the dam.

Below, some of the results obtained for the case in 2D are shown, although in the future it is wanted to reach 3D, for this it will be necessary to improve several aspects.
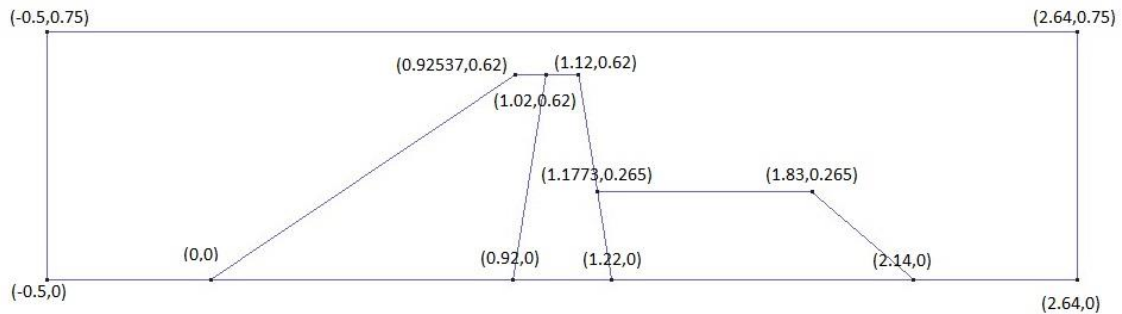

Figure 28: Geometry of the dam model

	Clay	Rockfill
Density (kg/m3)	1920	200000
Thickness	1	1
Young Modulus	1000000	1000000
Poisson ratio	0,29	0,29
Cohesion	5000	0
Internal friction angle	0,436332313	0,645771823
Internal dilatancy angle	0	0

Table 10: Properties of the materials.

| *Initial time*	0
Time step	0,001
Final time	1

Table 11: Times used for the calculations.

Below is shown the deformation of the dam's clay core in different steps when the water is impacting on it with a push acceleration (using volumetric accelerations). For now, it has been possible to simulate the core's fracture in 2D and it is being investigated in 3D but the cohesion effects much more in the three-dimensional case, so it will be necessary to continue

investigating in order to obtain considerable results. The results are shown in the two-dimensional model and later in the three-dimensional model.

4.2.1 Two-dimensional dam model

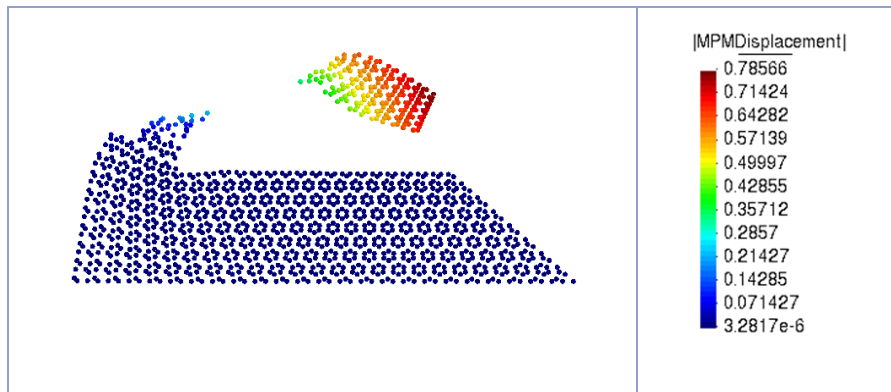At first it is shown the results of the deformation obtained for different time steps:
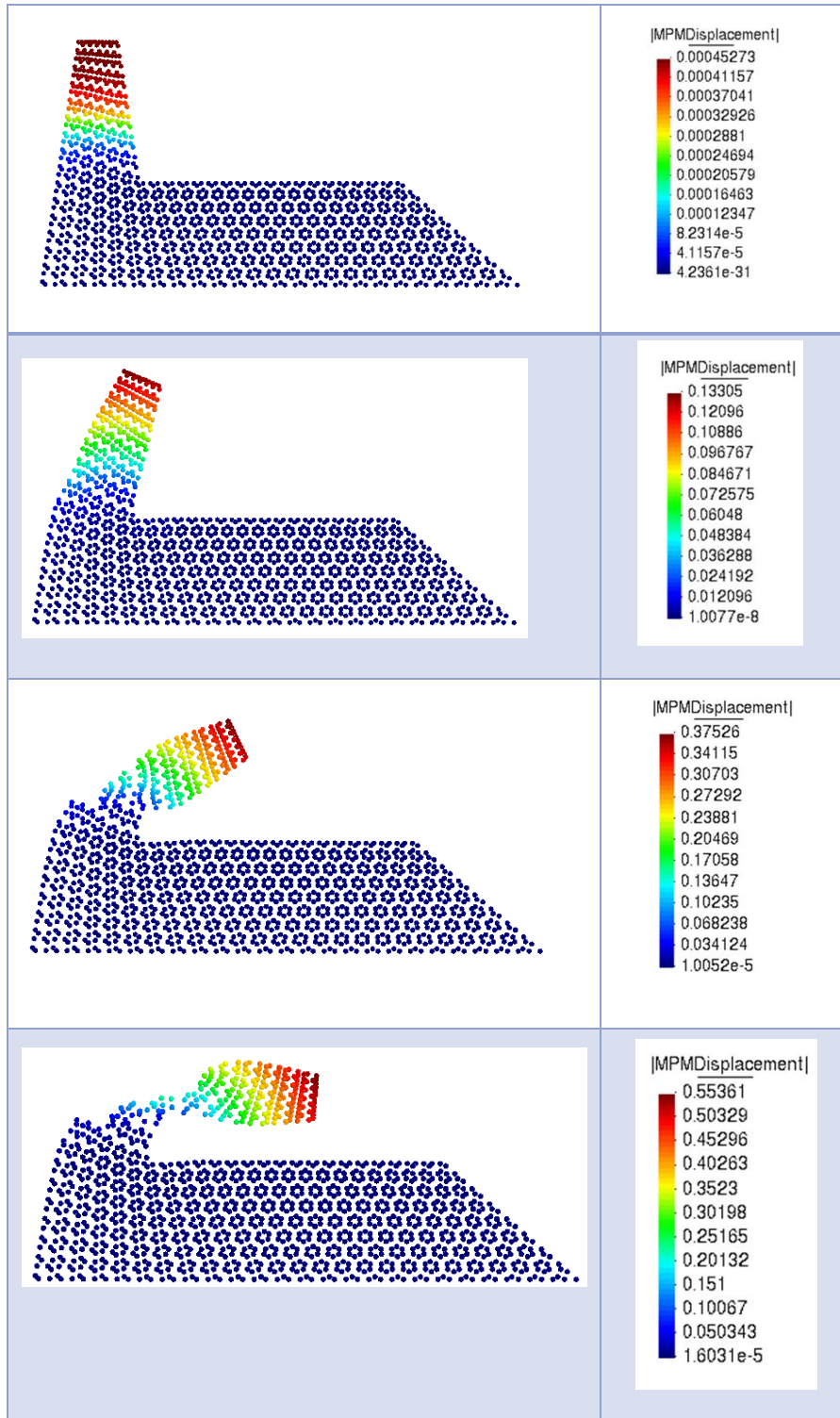
Figure 29: Results obtained in the analysis for different time steps.

It is observed that as the water pushes on the coronation of the dam, the core is displaced, reaching an increasing deformation until the core breaks.

It is necessary to emphasize that in the analysis there are different things that do not work and that it is necessary to correct, when applying the volumetric acceleration and once the nucleus has fractured, it moves to the right without falling. It is as if the gravitational force did not act, this must be corrected in the future because this push would indeed break the prey, but the piece that would come off would not only be fired to the right, but would also fall by its own weight since the force of gravity acts.

In addition to the results in terms of displacements, results of how plasticizes the structure to understand how the fracture occurs are shown.
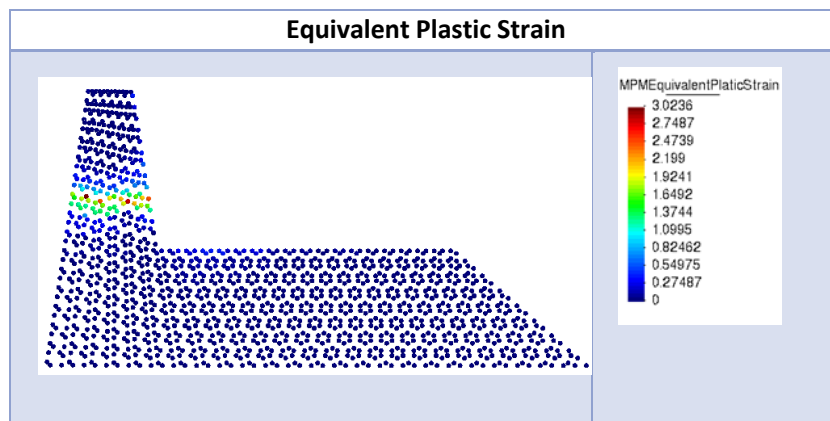

Figure 30: Equivalent Plastic Strain for 2D dam simulation.

Effectively it is observed that in the zone in which the plasticization takes place, it is just where the core breaks. In the following image the horizontal displacement is shown to get an idea of how is that fracture.

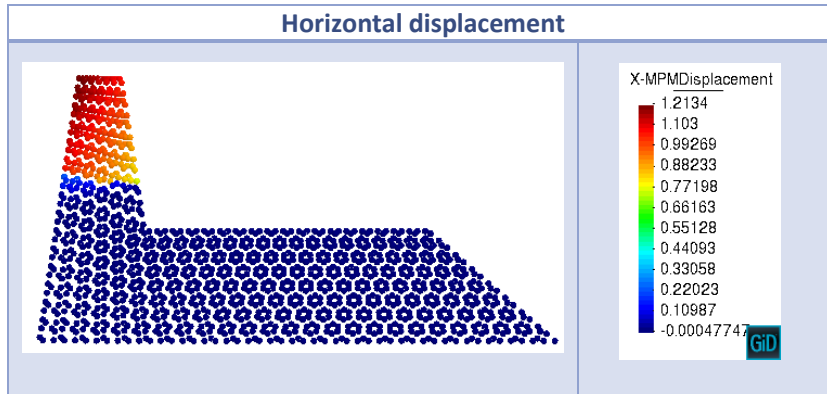## Horizontal displacement

Figure 31: Horizontal displacement for 2D dam simulation.
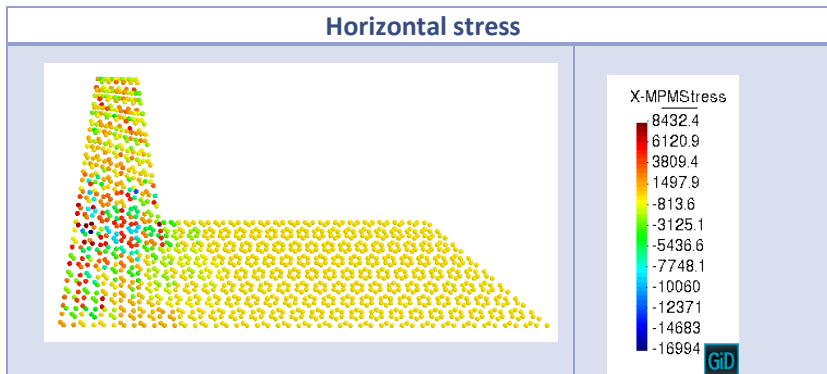
Horizontal stress

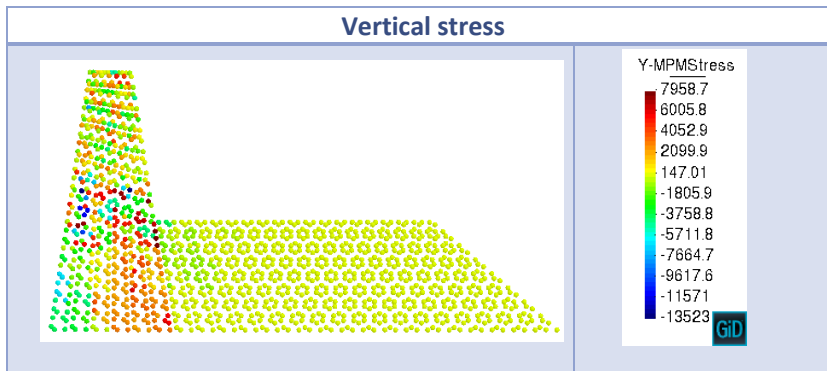**Figure 32: Horizontal stress for 2D dam simulation.**

Vertical stress

Figure 33: Vertical stress for 2D dam simulation.

'

Conclusions and future work

The MPM formulation presented works, although some aspects need to be improved, the mesh dependence on the direction of fracture as well as the contact surfaces on these materials. To obtain good results in this type of simulations, as in the case of the dam, it would be necessary to implement a contact algorithm.

As we have seen in the case of the dam, the method needs to be improved so to evaluate functional contact. To improve contact and fracture in the Material Point Method, enrichment or division of the mesh-scale material in different velocity fields is required to allow displacement or speed discontinuities in a material interface.

As is known, the material point method is very suitable for large deformation problems in solid mechanics and it is interesting to study for solving important engineering problems in the future. In general, we it can be said that the Material Point Method implemented in *Kratos Multiphysics* works correctly, obtaining promising results for the validation case.

The results obtained with damage models show the characteristics of the method, some of them expected. It is observed that as a higher number of material points and a finer mesh is used, a better approximation to the experimental solution is obtained. In addition, the calculation times for the simulations are not large, which is very useful in order to observe more quickly how the analysis occurs and to be able to modify some parameter if it is necessary.

The precision in 3D in the validation with models of damage is better than the one obtained in 2D, which is also expected given that the 3D simulations are more realistic. Although the different 2D tests are useful because they offer a fairly approximate view of how the code behaves in our analysis. In spite of this, good results for the three-dimensional dam case have not been achieved because cohesion plays a much more important role in 3D.

As a conclusion, it can be said that a fairly broad knowledge of this method has been acquired, despite not been able to reach the fracture of the dam as was originally wanted. It is aware that there is a need to improve different aspects such as the mesh dependence and a contact algorithm able to avoid crossing errors as well as extension instabilities that lead to numerical (non-physical) fractures.

A promising solution is the convective particle domain interpolation (CPDI), in which the integration domain used to map data between particles and the background grid deforms with the particle, based on the material deformation gradient. While eliminating the extension instability can be a benefit, it is often desirable to allow material separation to avoid nonphysical stretching.

Bibliography

[1] I. AL-Kafaji, Formulation of a dynamic material point method (MPM) for geomechanical problems. (2013). Ph.D. thesis, Institut für Geotechnik der Universität Stuttgart.

[2] E. Alonso, A. Yerro and N. Pinyol, January 2013. "The Material Point Method: A promising computational tool in Geotechnics ". 18th International Conference for Soil Mechanics and Geotechnical Engineering, At Paris. UPC Commons.

[3] S. Bardenhagen and M. Kober, The generalized material point method. ComputerModeling in Engineering and Sciences 5, p. 477 (2004).

[4] S.G. Bardenhagen, J.U. Brackbill , D. Sulsky (2000): The Material Point Method for granular materials. Comput. Methods Appl. Mech. Engrg. 187 (2000) 529-541

[5] S.G. Bardenhagen, J.E Guilkey, K.M Roessig, J.U. Brackbill , W.M. Witzel and J.C. Foster (2001): An Improved Contact Algorithm for the Material Point Method and Application to Stress propagation in Granular Material. CMES, vol.2, no.4, pp.509-522,2001

[6] T.B. Belytschko, J.M. Kennedy, Computer models for subassembly simulation, Nuclear Engineering and Design 49 (1978) 17–38.

[7] L. Beuth, Formulation of a Quasi-StaticMaterial PointMethod, Ph.D. thesis, Universität Stuttgart (2012).

[8] Y. Bing, M. Cortis, T. Charlton, W. Coombs and C. Augarde (2017). "Boundary representation and boundary condition imposition in the material point method". Proceedings of the 25th UKACM Conference on Computational Mechanics. 12-13 April 2017, University if Birmingham, United Kingdom.

[9] J.U. Brackbill, D.B. Kothe, H.M. Ruppel, FLIP: A low-dissipation, particle-in-cell method for fluid flow, Computer Physics   48 (1988) 25–38.

[10] J.U. Brackbill, H.M. Ruppel, FLIP: A method for adaptively zoned, particle-in-cell calculations of fluid flows in two dimensions, Journal of Computational Physics 65 (1986) 314–343

[11] CIMNE, Informe de Resultados. Fabricación y caracterización de Hormigones H30 y H50. Barcelona, 17/04/2015. LTE/TGV/0415-24

[12] B. Chandra, A. Larese, I. Iaconeta, R. Rossi and R. Wüchner. (2018) "Soil-structure interaction simulation of landslides impacting a structure using an implicit material point method".

[13] Z. Chen and R. Brannon 2002. "An Evaluation of the Material Point Method". Sand Report sand2002-0482, Feb 2002, Sandia National laboratories.

[14] Z. P. Chen, X. Zhang, X. M. Qiu and Y. Liu (2017). " A Frictional contact algorithm for implicit material point method". Computer Methods in Applied Mechanics and Engineering. Volume 321, 1 July 2017, pages 124-144.

[15] C.J. Coetzee, A.H. Basson and P.A. Vermeer (2006). "Discrete and Continuum Modelling of the Silo Discharge". R&D Journal, A Publication of the South African Institution of Mechanical Engineering, 2006, 22(2):26-38.

[16] R. F. Craig (2004). Craig's soil mechanics. London. Spon press

[17] J. Donea, A. Huerta, J.-P. Ponthot, A. Rodríguez-Ferran, Arbitrary Lagrangian–Eulerian methods, in: Encyclopedia of Computational Mechanics, John Wiley & Sons, 2004.

[18] Escuela de Ingenieros de Caminos, Canales y Puertos de la Universidad Politécnica de Madrid, 2011. Shear Test:
http://www2.caminos.upm.es/Departamentos/construccion/Materiales/webmat/InstalacionesF.h
m

[19] I. Fernandes, Exploring quadratic shape functions in material point method, Ph.D. thesis, University of Utah, year = 2004.

[20] R.M. Frank, R.B. Lazarus, Mixed Eulerian–Lagrangian method, in: B. Alder, S. Fernbach, M. Rotenberg (Eds.), Methods in Computational Physics, Vol. 3: Fundamental Methods in Hydrodynamics, Academic Press, New York, 1964, pp. 47–67.

[21] R.A. Gingold, J.J. Monaghan, Smoothed particle hydrodynamics: Theory and application to nonspherical stars, Monthly Notices of the Royal Astronomical Society 18 (1977) 375–389.

[22] M. Gong, Improving the Material PointMethod. (2015). Ph.D. thesis, The University of NewMexico.

[23] Guilkey, J.E.;Weiss, J.A. Implicit time integration for the material point method: Quantitative and algorithmic comparisons with the finite element method. Int. J. Numer. Methods Eng. 2003, 57, 1323–1338, doi:10.1002/nme.729.

[24] J. Guilkey, J. Hoying, and J.Weiss, Computational modeling of multicellular constructs with the material point method, Journal of Biomechanics 39, p. 2074 (2006).

[25] F. Hamad, D. Stolle, and P. Vermeer, Modelling of membranes in the material point method with applications, International Journal for Numerical and AnalyticalMethods in Geomechanics 39, p. 833 (2015).

[26] F.H. Harlow, A machine calculation method for hydrodynamic problems, Tech. Rep. LAMS-1956, Los Alamos Scientific Laboratory, 1955.

[27] F.H. Harlow, Hydrodynamic problems involving large fluid distortions, Journal of the ACM 4 (1) (1957) 137–142.

[28]. F.H. Harlow, The particle-in-cell computing method for fluid dynamics, Methods in Computational Physics 3 (1964) 319–343.

[29] F.H. Harlow, J.E. Welch, Numerical calculation of time-dependent viscous incompressible flow of fluid with a free surface, Physics of Fluids 8 (1965) 2182–2189.

[30] F.H. Harlow, Fluid dynamics in group T-3 Los Alamos National Laboratory (LA-UR- 03-3852), Journal of Computational Physics 195 (2004) 414–433.

[31] T.J.R. Hughes,W.K. Liu, T.K. Zimmermann, Lagrangian–Eulerian finite element formulation for incompressible viscous flows, Computer Methods in Applied Mechanics and Engineering 29 (3) (1981) 329–349.

[32] I. Iaconeta. CIMNE (2016). International Journal for Numerical methods in Engineering, (2016), 00:1-24 Published online in Wiley Online Library (wileyonlinelibrary.com). DOI: 10.1002/nme

[33] I. Iaconeta, A. Larese, R. Rossi and Z. Guo. CIMNE (2017) "Comparison of a displacement-based and a stabilized mixed formulation within the framework of the Material Point Method". Materials 2017, 10, 1150

[34] I. Iaconeta, A. Larese, R. Rossi and E. Oñate. (2017). "An implicit material point method applied to granular flows". Procedia Engineering 175 (2017) 226-232.

[35] N.L. Johnson, The legacy and future of CFD at Los Alamos, Tech. Rep. LA-UR- 96-1426, 1996.

[36] E. G. Kakouris, S. P. Triantafyllou (2017) "Phase-field material point method for brittle fracture". International Journal for Numerical Methods in Engineering, 112 (12). pp. 1750-1776. ISSN 1097-0207

[37] S. Kularathna and K. Soga (2017). "Projection Method in Material Point Method for Modelling Incompressible Materials". Procedia Engineering. Volume 175, 2017, pages 57-64.

[38] J. Lemaitre. A Continuous Damage Mechanics Model for Ductile Fracture. Journal of Engineering Materials and Technology. January 1985, Vol. 107/89.

[39] J. Lemaitre. Handbook of Materials Behavior Models, 2, Elsevier, pp.500-512, 2001, Failures of materials, 978-0-12-443341-0. 〈10.1016/B978-012443341-0/50056-9〉

[40] Lima Araujo, Daniel & Gabrielle Tiburcio Nunes, Fernanda & Toledo Filho, Romildo & Alexandre Souza de Andrade, Moacir. (2014). Shear strength of steel fiber-reinforced concrete beams. Acta Scientiarum Technology. 36. 389-397. 10.4025/actascitechnol.v36i3.19005.

[41] L.B. Lucy, A numerical approach to the testing of the fission hypothesis, The Astrophysical 8 (12) (1977) 1013–1024.

[42] L. Malvern, Introduction to the Mechanics of a Continious Medium(Pearson, 1977).

[43] S. Ma, X. Zhang, X.M. Qiu, Comparison study of MPM and SPH in modeling hypervelocity impact problems, International Journal of Impact Engineering 36 (2009) 272–282.

[44] Mazars, J. (1984) Application of Continuous Damage Mechanic to Non-Linear Behavior of Concrete Structures. PhD Thesis, Paris 6 University, Paris.

[45] S. McKee, M.F. Tomé, V.G. Ferreira, et al., The MAC method, Computers & Fluids 37 (8) (2008) 907–930.

[46] M.Möller, Flow models and governing equations, (Lecture slides) .

[47] Y.G. Motlagh and W. M. Coombs (2017). "An Implicit High-order Material Point Method" Procedia Engineering. Volume 175, 2017, pages 8-13.

[48] J.A. Nairn (2003): Material Point Method Calculations with Explicit Cracks. CMES, vol.4, no.6, pp.649-663, 2003

[49] A. Nishiguchi, T. Yabe, Second order fluid particle scheme, Journal of Computational Physics 52 (1983) 390–413.

[50] W.F. Noh, CEL: A time-dependent, two-space-dependent, coupled Euler–Lagrange code, Methods in Computational Physics 3 (1964) 117–179.

[51] M. Steffen, R. Kirby, and M. Berzins, Analysis and reduction of quadrature errors in the material point method (mpm). International journal for numerical methods in engineering 76, p. 922 (2008).

[52] M. Stojek and J. Pietraszek, "Simulation-Based Engineering Science Challenges of the 21st Century", Applied Mechanics and Materials, Vol. 712, pp. 3-8, 2015

[53] A. Stomakhin, C. Schroeder, L. Chai, J. Teran, and A. Selle, A material point method for snow simulation, ACM Transactions on Graphics 32 (2013).

[54] D. Sulsky, J. Brackbill, and D. Burgess, Mass matrix formulation of the flip particle-in-cell method. Journal Computational Physics, Volume 103, Issue 1, 1992, pages 1-15.

[55] D. Sulsky, Z. Chen, H.L. Schreyer, A particle method for history-dependent materials, Computer Methods in Applied Mechanics and Engineering 118 (1–2) (1994) 179–196.

[56] D. Sulsky and H. Schreyer, Axisymmetric form of the material point method with applications to upsetting and taylor impact problems. ComputerMethods in AppliedMechanics an Engineering 139, p. 409 (1996).

[57] D. Sulsky, H. Schreyer, K. Peterson, R. Kwok, and M. Coon, Using the material-point method to model sea ice dynamics, Journal of Geophysical Research 112 (2007).

[58]. Sulsky, D.; Zhou, S.J.; Schreyer, H.L. Application of a particle-in-cell method to solid mechanics. Comput. Phys. Commun. 1995, 87, 236–252, doi:10.1016/0010-4655(94)00170-7.

[59] J. Tao, Y. Zheng, Z. Chen and H. Zhang (2016). "Generalized interpolation material point method for coupled thermo-mechanical processes". International Journal of Mechanics and Materials in Design, December 2016, Volume 12, Issue 4, pp 577–595

[60] R. Tielen, E. Wobbes, M. Moller and L. Beuth (2017). "A High Order Material Point Method". Procedia Engineering, Volume 157, 2017, pages 265-272.

[61] Wang, B.; Vardon, P.; Hicks, M.; Chen, Z. Development of an implicit material point method for geotechnical applications. Comput. Geotech. 2016, 71, 159–167.

[62] Z. Wieckowski (2004). "The material point method in large strain engineering problems". Comput. Methods Appl. Mech. Engrg, 193 (2004) 4417-4438.

[63] Wikipedia: Continuum Mechanics, Motion of a continuum body. January 2011: https://es.wikipedia.org/wiki/Archivo:Continuum_body_deformation.svg

[64] Wikimedia Commons, Dcember 2016: Concrete Compression Testing: https://commons.wikimedia.org/wiki/File:Concrete_Compression_Testing.jpg

[65]. Wriggers, P. Computational Contact Mechanics; Springer: Berlin, Germany, 2006; p. 521 (tinc dubtes de si nombra ecu o ref)

[66] D. Zhang, X. Ma, and P. Giguere, Material point method enhanced by modified gradient of shape function,4Journal of Computational Physics 230, 6379 (2011).

[67] D. Zhang, Q. Zou, B. VanderHeyden, and X. Ma, Material point method applied to multiphase flows, Journal of Computational Physics 227, p. 3159 (2008).